GEOPHYSICS, VOL. 75, NO. 1 (JANUARY-FEBRUARY 2010); P. F33–F50, 14 FIGS., 2 TABLES.
10.1190/1.3278525

High-order finite-difference simulations of marine CSEM surveys using a correspondence principle for wave and diffusion fields

Rune Mittet[1]

ABSTRACT

The computer time required to solve a typical 3D marine controlled-source electromagnetic surveying (CSEM) simulation can be reduced by more than one order of magnitude by transforming low-frequency Maxwell equations in the quasi-static or diffusive limit to a hyperbolic set of partial differential equations that give a representation of electromagnetic fields in a fictitious wave domain. The dispersion and stability analysis can be made equivalent to that of other types of wave simulation problems such as seismic acoustic and elastic modeling. Second-order to eighth-order spatial derivative operators are implemented for flexibility. Fourth-order and sixth-order methods are the most numerically efficient implementations for this particular scheme. An implementation with high-order operators requires that both electric and magnetic fields are extrapolated simultaneously into the air layer. The stability condition given for high-order staggered-derivative operators here should be equally valid for seismic-wave simulation. The bandwidth of recovered fields in the diffusive domain is independent of the bandwidth of the fields in the fictitious wave domain. The fields in the fictitious wave domain do not represent observable fields. Propagation paths and interaction/reflection amplitudes are not altered by the transform from the fictitious wave domain to the diffusive frequency domain; however, the transform contains an exponential decay factor that damps down late arrivals in the fictitious wave domain. The propagation paths that contribute most to the diffusive domain fields are airwave (shallow water) plus typically postcritical events such as refracted and guided waves. The transform from the diffusive frequency domain to the fictitious wave domain is an ill-posed problem. The transform is nonunique. This gives a large degree of freedom in postulating temporal waveforms for boundary conditions in the fictitious wave domain that reproduce correct diffusive frequency-domain fields.

INTRODUCTION

Marine controlled-source electromagnetic (CSEM) surveying is now an established technique for hydrocarbon exploration (Eidesmo et al., 2002; Ellingsrud et al., 2002; Srnka et al., 2006). Marine CSEM methods use an electric dipole transmitter to probe the subsurface. The technique has proven particularly useful for detecting thin, highly resistive layers typical to hydrocarbon reservoirs. Three-dimensional modeling plays an important role in marine CSEM both for survey design and inversion of observed data. These two areas have in common the necessity for a large number of 3D simulations. Proper survey design requires modeling of each receiver location for a multitude of frequencies and subsurface scenarios. It is not uncommon to analyze 10 or more frequencies in the range 0.1 Hz to 3–5 Hz in the pre-survey study.

A time-domain modeling scheme can compute the electromagnetic fields for these frequencies in one run whereas a frequency-domain scheme must model the field for each frequency in separate runs. Reciprocity can be used to reduce the modeling time significantly. The source location in the modeling operation is then at the true receiver location and the modeled data is recorded at the true source positions. The simulation of each electric or magnetic component requires a separate modeling run because reciprocity dictates different electric or magnetic dipole source functions for these components. Thus, approximately 100 3D modeling operations for a line layout of 25–30 receivers could be required, even if all relevant frequencies for a given receiver and subsurface realization can be extracted from one modeling operation. Two to four times more receivers must be analyzed for a small 3D data set. Three-dimensional inversion is several orders of magnitude more computer intensive.

Marine CSEM is a low-frequency method. This implies that displacement currents are negligible and that the analysis of the experiment can be carried out in the diffusive or quasi-static limit. It is well established that the finite-difference time-domain (FDTD) solution of the Maxwell equations in the purely diffusive limit is time consuming, mainly resulting from the fact that the stability condition dictates a very small time step (Oristaglio and Hohmann, 1984; Wang and Hohmann, 1993). Both Oristaglio and Hohmann (1984)

Manuscript received by the Editor 31 March 2009; revised manuscript received 22 June 2009; published online 2 February 2010.
[1]EMGS AS, Trondheim, Norway. E-mail: rm@emgs.com.

and Wang and Hohmann (1993) observe that the computer time can be reduced by introducing a small wavelike contribution in the solution by the DuFort-Frankel method. Maaø (2007) proposes a transformation method that reduces CPU time by a factor of 40 compared to a fixed time-step DuFort-Frankel–based scheme and a factor of 10 compared to a variable time-step DuFort-Frankel–based scheme. The method proposed by Maaø (2007) is related closely to the FDTD method introduced by Lee et al. (1989) and more formally discussed by de Hoop (1996) as a correspondence principle for time-domain electromagnetic wave and diffusion fields. The potential benefit of these transform methods is that they can reduce CPU time for 3D simulations using finite-difference or finite-element techniques.

The focus of this paper is on 3D FDTD simulations of the Maxwell equations for marine CSEM exploration but some of the results might carry over to other finite-difference applications. As mentioned, a key goal in 3D FDTD simulations is to have a numerically cost-effective scheme. To achieve this for the Maxwell equations, it turns out that time integration is the critical factor. The solution must be stable, which puts constraints on the maximum allowed time step in an explicit scheme. If the term giving rise to the displacement currents is included in the solution then the highest propagation velocity will be the velocity of light. A very small time step is then required to satisfy Courant-Friedrichs-Lewy (CFL) or von Neumann stability conditions.

The term giving rise to the displacement current can be neglected for low-frequency field propagation in a conductive medium. This gives solutions to the Maxwell equations in the quasi-static or diffusive limit that are sufficiently accurate for marine CSEM applications. However, the problem of a small time step remains. The Maxwell equations in the diffusive limit have solutions on very different timescales. A system of partial differential equations can be considered stiff if this is the case. The straightforward explicit numerical integration of a stiff system of partial differential equations requires a very fine time step.

The time integration of the Maxwell equations is discussed thoroughly in Oristaglio and Hohmann (1984). They propose to use the DuFort-Frankel method, adding a hyperbolic term to the diffusive Maxwell equations. This gives a damped wave equation that is unconditionally stable with the upper time-step limit given by the classic CFL condition. The DuFort-Frankel method must be used with care because the wavelike solutions must be kept much smaller than the diffusive solutions. This limits the size of the time step as smaller than the time step dictated by the stability condition.

A modified DuFort-Frankel method was introduced by Wang and Hohmann (1993), in which the term giving rise to the displacement current was kept for the Maxwell equations. The dielectric permittivity was set to 2700 times the vacuum value, effectively reducing the velocity of light and allowing for an increased time step. However, the fictitious displacement currents must be kept sufficiently small to prevent them from dominating the diffusive EM field. Again, this limits the size of the time step as smaller than the time step dictated by the stability condition. On the other hand, they state that with this modified DuFort-Frankel method, the time step can be increased at later times when the fields are smoothed out. This is a recipe for an additional reduction in CPU time.

Commer and Newman (2006) take this approach one step further by realizing that the smooth fields at later times can be represented properly on a grid coarser than the initial grid. They propose one or two regridding operations as time increases. This can reduce the CPU time by a factor of up to five. Carcione (2006) proposes a completely different approach to time integration. This method is based on a Chebychev expansion for time evolution. The scheme has the numerical accuracy of order machine precision and the stability condition allows for large time steps. Each time step is more costly to calculate than for a low-order scheme.

The above methods give solutions to the Maxwell equations that require no postprocessing of the modeling results. Maaø (2007) proposes a scheme that uses a larger hyperbolic term than Wang and Hohmann (1993). The time-domain solution can no longer be regarded as representing real fields. However, he demonstrates that proper frequency-domain diffusive EM fields can be obtained by a postprocessing step. I show in Appendix A that his method is a step toward applying the correspondence principle for wave and diffusion fields (Lee et al., 1989; de Hoop, 1996; Gershenson, 1997) to the diffusive Maxwell equations.

The diffusive Maxwell equations are transformed to a set of hyperbolic Maxwell equations by the application of the correspondence principle. The resulting EM fields become completely wavelike. However, these fields are not real observable fields. They are "containers" that hold the necessary information from the simulation process. Proper frequency- and time-domain diffusive solutions can be obtained by postsimulation frequency- and time-domain transforms. A single transform is sufficient to obtain frequency-domain solutions. A double transform is required to obtain diffusive time-domain solutions. The potential benefit of transforming the diffusive Maxwell equations to a fictitious wave domain is reducing CPU time.

First, a relatively large time step can be used because a hyperbolic set of partial differential equations is solved. The transform that takes the data from the fictitious wave domain to the frequency domain has the property that it is the early arrivals in the fictitious wave domain that dominates the proper diffusive solution in the frequency domain. This limits the number of time steps required in the FDTD simulation and, hence, reduces numerical cost. The combination of a relatively large time step and a relatively short required simulation time makes modeling in the fictitious wave domain a numerically efficient method. Proper diffusive time-domain solutions can be reconstructed from diffusive frequency-domain solutions.

THEORY

I prefer to use a formulation similar to de Hoop (1996) for the derivation of the wave-domain equation, with the difference that I use Fourier transforms instead of Laplace transforms. The derivation introduces an arbitrary circular frequency ω_0, which corresponds to the parameter α in de Hoop (1996). This has the effect that the time axis in the fictitious wave domain is still in units of s and velocity is in units of m/s. This differs from Lee et al. (1989), who have a timelike axis, denoted q, which is in units of the square root of seconds ($\sqrt{\text{s}}$) and velocities in units of meters per the square root of seconds ($\text{m}/\sqrt{\text{s}}$). I choose a formulation with velocity in units of m/s and time in units of s because the dispersion and stability analysis becomes identical to that of a standard FDTD wave simulation. The two representations are related in Appendix B and they give the same results when the wave-domain solutions are transformed to the diffusive domain. The Green's functions in the diffusive domain are independent of the value of ω_0 for the fictitious wave domain. The effect of this choice is removed in the transforms from the wave domain to the diffusive domain.

I use the following set of Fourier transforms:

$$f(\omega) = \int_0^T dt f(t) e^{i\omega t},$$

$$f(t) = \frac{1}{2\pi}\int_{-\omega_N}^{\omega_N} d\omega f(\omega) e^{-i\omega t}. \quad (1)$$

The underlying assumption here is that all sources and fields analyzed in the following are causal in the sense that they have a zero or a negligible contribution for $t \le 0$.

From the diffusive domain to the fictitious wave domain, the quasi-static Maxwell equations in the time domain are

$$-\nabla \times \boldsymbol{H}(\boldsymbol{x},t) + \boldsymbol{\sigma}(\boldsymbol{x})\boldsymbol{E}(\boldsymbol{x},t) = -\boldsymbol{J}(\boldsymbol{x},t),$$
$$\nabla \times \boldsymbol{E}(\boldsymbol{x},t) + \mu\partial_t \boldsymbol{H}(\boldsymbol{x},t) = -\boldsymbol{K}(\boldsymbol{x},t), \quad (2)$$

where $\boldsymbol{E}$ and $\boldsymbol{H}$ are electric and magnetic vector fields, respectively. The source terms are electric current density $\boldsymbol{J}$ and magnetic current density $\boldsymbol{K}$. The conductivity tensor is $\boldsymbol{\sigma}$. The FDTD implementation is TIV anisotropic so that only diagonal elements of the conductivity tensor differ from zero. The magnetic permeability μ is assumed to be isotropic and constant.

The frequency-domain representation is

$$-\nabla \times \boldsymbol{H}(\boldsymbol{x},\omega) + \boldsymbol{\sigma}(\boldsymbol{x})\boldsymbol{E}(\boldsymbol{x},\omega) = -\boldsymbol{J}(\boldsymbol{x},\omega),$$
$$\nabla \times \boldsymbol{E}(\boldsymbol{x},\omega) - i\omega\mu\boldsymbol{H}(\boldsymbol{x},\omega) = -\boldsymbol{K}(\boldsymbol{x},\omega). \quad (3)$$

The hyperbolic representation of the Maxwell equations is given by

$$-\nabla \times \boldsymbol{H}(\boldsymbol{x},t) + \boldsymbol{\epsilon}(\boldsymbol{x})\partial_t \boldsymbol{E}(\boldsymbol{x},t) = -\boldsymbol{J}(\boldsymbol{x},t),$$
$$\nabla \times \boldsymbol{E}(\boldsymbol{x},t) + \mu\partial_t \boldsymbol{H}(\boldsymbol{x},t) = -\boldsymbol{K}(\boldsymbol{x},t), \quad (4)$$

where $\boldsymbol{\epsilon}$ is the dielectric permittivity tensor. Equation 4 has the following frequency-domain representation:

$$-\nabla \times \boldsymbol{H}(\boldsymbol{x},\omega) - i\omega\boldsymbol{\epsilon}(\boldsymbol{x})\boldsymbol{E}(\boldsymbol{x},\omega) = -\boldsymbol{J}(\boldsymbol{x},\omega),$$
$$\nabla \times \boldsymbol{E}(\boldsymbol{x},\omega) - i\omega\mu\boldsymbol{H}(\boldsymbol{x},\omega) = -\boldsymbol{K}(\boldsymbol{x},\omega). \quad (5)$$

In the following, I will use a notation in which parameters and fields that are particular for the fictitious wave domain are primed. I start with equation 3 and define a fictitious dielectric permittivity tensor $\boldsymbol{\epsilon}'$ from the conductivity tensor by

$$\boldsymbol{\sigma}(\boldsymbol{x}) = 2\omega_0\boldsymbol{\epsilon}'(\boldsymbol{x}) \quad (6)$$

to obtain

$$-\nabla \times \boldsymbol{H}(\boldsymbol{x},\omega) + 2\omega_0\boldsymbol{\epsilon}'(\boldsymbol{x})\boldsymbol{E}(\boldsymbol{x},\omega) = -\boldsymbol{J}(\boldsymbol{x},\omega),$$
$$\nabla \times \boldsymbol{E}(\boldsymbol{x},\omega) - i\omega\mu\boldsymbol{H}(\boldsymbol{x},\omega) = -\boldsymbol{K}(\boldsymbol{x},\omega). \quad (7)$$

The equation for Ampère's law is multiplied by the term

$$\sqrt{\frac{-i\omega}{2\omega_0}}, \quad (8)$$

which gives

$$-\nabla \times \left[\sqrt{\frac{-i\omega}{2\omega_0}}\boldsymbol{H}(\boldsymbol{x},\omega)\right] + \sqrt{-2i\omega\omega_0}\boldsymbol{\epsilon}'(\boldsymbol{x})\boldsymbol{E}(\boldsymbol{x},\omega)$$
$$= -\sqrt{\frac{-i\omega}{2\omega_0}}\boldsymbol{J}(\boldsymbol{x},\omega),$$
$$\nabla \times \boldsymbol{E}(\boldsymbol{x},\omega) + \sqrt{-2i\omega\omega_0}\mu\left[\sqrt{\frac{-i\omega}{2\omega_0}}\boldsymbol{H}(\boldsymbol{x},\omega)\right]$$
$$= -\boldsymbol{K}(\boldsymbol{x},\omega). \quad (9)$$

First, I identify ω' by

$$-i\omega' = \sqrt{-2i\omega\omega_0},$$
$$\omega' = (i+1)\sqrt{\omega\omega_0}, \quad (10)$$

which will be used in the transforms of the fields from the temporal but fictitious wave domain to the frequency domain.

Second, I need to choose a scaling for the electromagnetic fields and sources. A natural choice is

$$\boldsymbol{E}'(\boldsymbol{x},\omega') = \boldsymbol{E}(\boldsymbol{x},\omega),$$
$$\boldsymbol{H}'(\boldsymbol{x},\omega') = \sqrt{\frac{-i\omega}{2\omega_0}}\boldsymbol{H}(\boldsymbol{x},\omega),$$
$$\boldsymbol{J}'(\boldsymbol{x},\omega') = \sqrt{\frac{-i\omega}{2\omega_0}}\boldsymbol{J}(\boldsymbol{x},\omega),$$
$$\boldsymbol{K}'(\boldsymbol{x},\omega') = \boldsymbol{K}(\boldsymbol{x},\omega), \quad (11)$$

but a multitude of other choices are allowed as long as the relative ratio between fields and sources are preserved. One other example is

$$\boldsymbol{E}'(\boldsymbol{x},\omega') = \sqrt{\frac{-2\omega_0}{i\omega}}\boldsymbol{E}(\boldsymbol{x},\omega),$$
$$\boldsymbol{H}'(\boldsymbol{x},\omega') = \boldsymbol{H}(\boldsymbol{x},\omega),$$
$$\boldsymbol{J}'(\boldsymbol{x},\omega') = \boldsymbol{J}(\boldsymbol{x},\omega),$$
$$\boldsymbol{K}'(\boldsymbol{x},\omega') = \sqrt{\frac{-2\omega_0}{i\omega}}\boldsymbol{K}(\boldsymbol{x},\omega), \quad (12)$$

which comes from multiplying both sides of equation 9 by the factor $\sqrt{-2\omega_0/i\omega}$.

By using the definition in equation 10 and the scaling in equation 11, equation 9 becomes

$$-\nabla \times \boldsymbol{H}'(\boldsymbol{x},\omega') - i\omega'\boldsymbol{\epsilon}'(\boldsymbol{x})\boldsymbol{E}'(\boldsymbol{x},\omega') = -\boldsymbol{J}'(\boldsymbol{x},\omega'),$$
$$\nabla \times \boldsymbol{E}'(\boldsymbol{x},\omega') - i\omega'\mu\boldsymbol{H}'(\boldsymbol{x},\omega') = -\boldsymbol{K}'(\boldsymbol{x},\omega'), \quad (13)$$

which is the same as equation 5 except for the primes. The time-domain representation of equation 13 is

$$-\nabla \times \boldsymbol{H}'(\boldsymbol{x},t') + \boldsymbol{\epsilon}'(\boldsymbol{x})\partial_{t'}\boldsymbol{E}'(\boldsymbol{x},t') = -\boldsymbol{J}'(\boldsymbol{x},t'),$$
$$\nabla \times \boldsymbol{E}'(\boldsymbol{x},t') + \mu\partial_{t'}\boldsymbol{H}'(\boldsymbol{x},t') = -\boldsymbol{K}'(\boldsymbol{x},t'). \quad (14)$$

This is the equation solved by the FDTD approach. The dielectric permittivity tensor is modified by the application of the correspondence principle. It is clear that equation 14 will no longer give solutions in terms of observable fields. However, the resulting electric and magnetic fields contain sufficient information to recover the diffusive fields. If I assume the conductivity tensor is isotropic and equal to $\sigma(\boldsymbol{x})$ for all components, I find the propagation velocities in the fictitious wave domain $c(\boldsymbol{x})$ are

$$c(\boldsymbol{x}) = \sqrt{\frac{2\omega_0}{\mu\sigma(\boldsymbol{x})}}. \tag{15}$$

From the fictitious wave domain to the diffusive domain

The procedure is to first recover the diffusive frequency-domain Green's functions for electric and magnetic sources from the solutions of the hyperbolic problem in the fictitious wave domain. With these Green's functions at hand, electric and magnetic fields in the diffusive frequency-domain resulting from electric or magnetic sources can be calculated. I change to component notation to demonstrate this. The frequency-domain electric Green's function in the i-direction resulting from an electric source in the n direction $G^{EJ}_{in}(\mathbf{x},\omega|\mathbf{x}_s)$ can be found by first extracting the electric field and then the electric current by a complex Fourier integral. From equation 11, I have

$$E_i(\boldsymbol{x},\omega) = E'_i(\boldsymbol{x},\omega') = \int_0^T dt' E'_i(\boldsymbol{x},t')e^{i\omega' t'}, \tag{16}$$

or with equation 10,

$$E_i(\boldsymbol{x},\omega) = \int_0^T dt' E'_i(\boldsymbol{x},t')e^{-\sqrt{\omega\omega_0}t'}e^{i\sqrt{\omega\omega_0}t'}. \tag{17}$$

Note that this transform contains an exponential damping factor applied to the field calculated in the fictitious wave domain. Two effects are observable immediately: First, early arrivals in the fictitious wave domain contribute more to the response in the diffusive frequency domain than late arrivals resulting from the damping of late arrivals from the $e^{-\sqrt{\omega\omega_0}t'}$ factor. Second, the temporal frequency content of the product $E'_i(\boldsymbol{x},t')e^{-\sqrt{\omega\omega_0}t'}$ can be much higher than the temporal frequency content of $E'_i(\boldsymbol{x},t')$ itself. The consequence is that it is possible to recover high-frequency contributions to $E_i(\boldsymbol{x},\omega)$ even if the field in the fictitious wave domain $E'_i(\boldsymbol{x},t')$ is low frequency.

I am interested in the Green's function response so I assume the spatial part of the source function behaves as a Dirac distribution:

$$J'_n(\boldsymbol{x}_s,t') = \delta(\boldsymbol{x}-\boldsymbol{x}_s)J'^T_n(t'). \tag{18}$$

For the temporal part of the electric source contribution,

$$J^T_n(\omega) = \sqrt{\frac{-2\omega_0}{i\omega}}\int_0^T dt' J'^T_n(t')e^{-\sqrt{\omega\omega_0}t'}e^{i\sqrt{\omega\omega_0}t'}, \tag{19}$$

and the diffusive frequency-domain Green's function is then

$$G^{EJ}_{in}(\boldsymbol{x},\omega|\boldsymbol{x}_s) = \frac{E_i(\boldsymbol{x},\omega)}{J^T_n(\omega)}. \tag{20}$$

The diffusive time-domain representation of the Green's function is obtained by a standard Fourier transform:

$$G^{EJ}_{in}(\boldsymbol{x},t|\boldsymbol{x}_s,0) = \frac{1}{2\pi}\int_{-\omega_N}^{\omega_N} d\omega G^{EJ}_{in}(\boldsymbol{x},\omega|\boldsymbol{x}_s)e^{-i\omega t}. \tag{21}$$

The transformation from the fictitious wave domain to the diffusive domain impulse response has two important properties: The Green's function in the diffusive domain becomes independent of the scale parameter ω_0 and, as mentioned, the spectral width or maximum frequency that can be recovered in the diffusive domain is independent of the spectral width or maximum frequency in the fictitious wave domain. The requirements on the wave-domain signal are that it is causal and that the time integration includes all important arrivals. How this can happen is best explained by an example assuming a whole-space solution. In this case, there exist analytical solutions in both the time domain and the frequency domain and the effects of transforming from the fictitious wave domain to the diffusive domain are apparent. This is discussed in Appendix C.

FINITE-DIFFERENCE IMPLEMENTATION

All the parameters and fields discussed in this section are in the fictitious wave domain; therefore, the prime notation is not used. This simplifies the notation. The finite-difference scheme is implemented using high-order staggered operators for spatial differentiation. The forward and backward derivative operators in the n-direction, ∂_n^+ and ∂_n^-, with operator half-length L_n are given as

$$\begin{aligned}\partial_n^+\psi(m) = \partial_n\psi\left(m+\frac{1}{2}\right) &\approx \frac{1}{\Delta x_n}\sum_{l=1}^{L_n}\alpha_n(l)[\psi(m+l)\\ &\quad -\psi(m-(l-1))],\\ \partial_n^-\psi(m) = \partial_n\psi\left(m-\frac{1}{2}\right) &\approx \frac{1}{\Delta x_n}\sum_{l=1}^{L_n}\alpha_n(l)[\psi(m+(l\\ &\quad -1))-\psi(m-l)],\end{aligned} \tag{22}$$

where ψ represents either an electric or a magnetic field component. The index n can represent any of the three spatial directions and Δx_n is the step length in the n-direction. The distance in the n-direction is $x_n = (m-1)\Delta x_n$. Indices for the two other spatial directions are suppressed for simplicity. The notations $\partial_n\psi\left(m+\frac{1}{2}\right)$ and $\partial_n\psi\left(m-\frac{1}{2}\right)$ are used to indicate that the field derivatives are located at staggered node positions. The dimensionless operator coefficients $\alpha_n(l)$ can be found either from Taylor approximations or an optimization procedure (Holberg, 1987). The FDTD implementation is for operator half-lengths ranging from one to four. The user is free to choose the operator type prior to each run.

I use a standard Yee grid (Yee, 1966; Wang and Hohmann, 1993). Let

$$\begin{aligned}x &= (i-1)\Delta x,\\ y &= (j-1)\Delta y,\\ z &= (k-1)\Delta z,\end{aligned} \tag{23}$$

and

$$I = i + \frac{1}{2},$$
$$J = j + \frac{1}{2},$$
$$K = k + \frac{1}{2}. \tag{24}$$

I introduce

$$\eta_{xx}(I,j,k) = \varepsilon_{xx}^{-1}(I,j,k) = \frac{2\omega_0}{\sigma_{xx}(I,j,k)} = 2\omega_0\rho_{xx}(I,j,k),$$
$$\eta_{yy}(i,J,k) = \varepsilon_{yy}^{-1}(i,J,k) = \frac{2\omega_0}{\sigma_{yy}(i,J,k)} = 2\omega_0\rho_{yy}(i,J,k),$$
$$\eta_{zz}(i,j,K) = \varepsilon_{zz}^{-1}(i,j,K) = \frac{2\omega_0}{\sigma_{zz}(i,j,K)} = 2\omega_0\rho_{zz}(i,j,K) \tag{25}$$

for the three diagonal components of the conductivity tensor. Here, ρ is resistivity. However, the parameter averaging is performed on the conductivity tensor components. The discretized Maxwell equations are then

$$H_x^{n+\frac{1}{2}}(i,J,K) = H_x^{n-\frac{1}{2}}(i,J,K) - \Delta t\mu^{-1}[\partial_y^+ E_z^n(i,j,K) - \partial_z^+ E_y^n(i,J,k)],$$
$$H_y^{n+\frac{1}{2}}(I,j,K) = H_y^{n-\frac{1}{2}}(I,j,K) - \Delta t\mu^{-1}[\partial_z^+ E_x^n(I,j,k) - \partial_x^+ E_z^n(i,j,K)],$$
$$H_z^{n+\frac{1}{2}}(I,J,k) = H_z^{n-\frac{1}{2}}(I,J,k) - \Delta t\mu^{-1}[\partial_x^+ E_y^n(i,J,k) - \partial_y^+ E_x^n(I,j,k)], \tag{26}$$

and

$$E_x^{n+1}(I,j,k) = E_x^n(I,j,k) + \Delta t\eta_{xx}(I,j,k)\left[\partial_y^- H_z^{n+\frac{1}{2}}(I,J,k) - \partial_z^- H_y^{n+\frac{1}{2}}(I,j,K)\right],$$
$$E_y^{n+1}(i,J,k) = E_y^n(i,J,k) + \Delta t\eta_{yy}(i,J,k)\left[\partial_z^- H_x^{n+\frac{1}{2}}(i,J,K) - \partial_x^- H_z^{n+\frac{1}{2}}(I,J,k)\right],$$
$$E_z^{n+1}(i,j,K) = E_z^n(i,j,K) + \Delta t\eta_{zz}(i,j,K)\left[\partial_x^- H_y^{n+\frac{1}{2}}(I,j,K) - \partial_y^- H_x^{n+\frac{1}{2}}(i,J,K)\right], \tag{27}$$

where n represents a time index. The source contributions are added to the fields at each time step. The spatial part of the source terms are approximated by band-limited Dirac distributions.

Dispersion

Equation 14 constitutes a wave equation. Thus, results from dispersion and stability analysis of wave-propagation problems can be applied directly. I have chosen an implementation using high-order optimized difference operators (Holberg, 1987). These operators are designed to be staggered and are well adapted to be used with a Yee grid. Spatial dispersion control is part of the design procedure for these types of operators and the spatial dispersion can be kept at a controlled and very low level for properly designed operators. The optimization procedure results in operators that allow for a maximum coarseness of the simulation grid. In this sense, they are superior to high-order operators based on Taylor expansion. Coefficients for such operators are given in Table 1. These operators are designed not to exceed a relative error in group velocity of 0.003 (Holberg, 1987). Operators based on Taylor expansion are shown in Table 2.

Differentiation can be formally written as a convolution integral

$$\partial_x^+ \psi(x) \approx \int dx' D_x^+(x')\psi(x - x'). \tag{28}$$

A numerical implementation based on finite differences is approximate. The error depends on how this integral is truncated. I use the x-axis for an illustration. Let $D_x^+(k_x)$ be the true response of the operator

$$ik_x\psi(k_x) \approx iD_x^+(k_x)\psi(k_x). \tag{29}$$

The difference between k_x and $D_x^+(k_x)$ will be small for wavenumbers up to a critical wavenumber k_x^c. The critical wavenumber will

Table 1. Staggered derivative operators based on the Holberg optimization scheme. The operator half-length L ranges from one to four. The minimum required number of gridpoints per shortest wavelength, G_{lim}, is given for a relative group velocity error of 0.003.

L	G_{lim}	α_1	α_2	α_3	α_4
1	30.3	1.00235			
2	6.7	1.14443	−0.04886		
3	4.2	1.20282	−0.08276	0.00950	
4	3.4	1.23041	−0.10313	0.02005	−0.00331

Table 2. Staggered derivative operators based on Taylor expansion. The operator half-length L ranges from one to four. The minimum required number of grid points per shortest wavelength, G_{lim}, is given for a relative group velocity error of 0.003. This is a strict criterion compared to what is usually cited in the literature.

L	G_{lim}	α_1	α_2	α_3	α_4
1	40.0	1.00000			
2	10.4	1.12500	−0.04167		
3	6.6	1.17188	−0.06510	0.00469	
4	5.3	1.19629	−0.07975	0.00957	−0.00070

depend on the length of the operator, the design method for the operator, and the criterion used to calculate the discrepancy between desired response k_x and actual response $D_x^+(k_x)$. The wavenumber response of any staggered-difference operator can be written

$$D_x^+(k_x) = \sum_{l=1}^{L} \frac{2}{\Delta x}\alpha_x(l)\sin\left(\frac{2l-1}{2}k_x\Delta x\right). \tag{30}$$

Equation 30 is independent of the design procedure for the difference operator and is valid equally for operators based on optimization and operators based on Taylor expansion. The performance of a difference operator can be measured in terms of the parameter G_{lim}, which is the required number of grid points per shortest wavelength. If the critical wavenumber k_x^c is determined from an inspection of $D_x^+(k_x)$, then

$$G_{\text{lim}} = 2\frac{k_x^N}{k_x^c}, \tag{31}$$

where k_x^N is the Nyquist wavenumber. Observe that $G_{\text{lim}} = 2$ for a pseudospectral method where $k_x^c = k_x^N$. This implies that only two grid points per shortest wavelength are required to sample the field properly. A second-order scheme in space will have $G_{\text{lim}} \sim 10-40$, depending on how much accuracy is required. The sampling density has an upper limit if the operator type, the maximum frequency, and the smallest propagation velocity are given

$$\Delta x \le \frac{c_{\text{min}}}{f_{\text{max}} G_{\text{lim}}}. \tag{32}$$

Optimized operators will in general have a smaller G_{lim} than operators based on Taylor expansion. Also, G_{lim} is reduced with increased operator length. By comparing the spatial sampling criteria, we observe that if optimized operators are used then a coarser grid can be used. The factor goes from 1.33 for $L = 1$ to 1.56 for $L = 4$. This is for each dimension. This implies that for a 3D grid there is a factor of 2.5 to 4 possible to gain in reduced computer time by using optimized derivative operators compared to operators based on a Taylor expansion. In fact, the reduction in CPU time can be even larger because the stability criterion allows for a larger time step when the spatial step lengths increase. This is discussed further at the end of the next section.

Temporal dispersion must be treated on the same footing as spatial dispersion. The time step must be sufficiently small to have a stable calculation but an additional check is required to see if the sampling is sufficient to avoid temporal dispersion. It is crucial to preserve the mapping between field and excitation current for the deconvolution in equation 20 to be sufficiently accurate. There are no propagation/dispersion effects on the transformed transmitter current in equation 19. However, these effects must be controlled for the wave-domain electric field in equation 17. The sampling in time must be sufficiently fine to give the same accuracy as the space-domain operations. This is even more important for the scheme discussed here than for a standard wave-simulation scheme because temporal dispersion leads the signal (Dablain, 1986). The early arrivals dominate strongly compared to later arrivals in the transform from fictitious wave domain to diffusive frequency domain.

Stability

Both the electric and magnetic fields are described by a wave equation for a whole-space. Equation 14 takes the form

$$\nabla^2\psi(\boldsymbol{x},t) - \mu\varepsilon\partial_t^2\psi(\boldsymbol{x},t) = 0, \tag{33}$$

in a source-free region. Here, $\psi(\boldsymbol{x},t)$ is a component of the electric or magnetic field and ε is one of the diagonal components of $\boldsymbol{\epsilon}$. The highest propagation velocity c^{max} determines the time-step limit

$$c^{\text{max}} = \frac{1}{\sqrt{\mu\varepsilon^{\text{min}}}} = \sqrt{\frac{2\omega_0}{\mu\sigma^{\text{min}}}}, \tag{34}$$

where σ^{min} is the element of the diagonal conductivity tensor with the lowest value. I assume that $\psi(k_x,k_y,k_z)^n$ is the wavenumber representation of the electric or magnetic field in a constant and homogeneous medium at time step n. A second-order scheme in time takes the form (Gazdag, 1981)

$$\begin{bmatrix} \psi(k_x,k_y,k_z)^{n+1} \\ \psi(k_x,k_y,k_z)^n \end{bmatrix} = \begin{bmatrix} 2-\theta(k_x,k_y,k_z)^2 & -1 \\ 1 & 0 \end{bmatrix} \times \begin{bmatrix} \psi(k_x,k_y,k_z)^n \\ \psi(k_x,k_y,k_z)^{n-1} \end{bmatrix}, \tag{35}$$

with

$$\theta(k_x,k_y,k_z) = c^{\text{max}}\Delta t\sqrt{D_x^2(k_x) + D_y^2(k_y) + D_z^2(k_z)}, \tag{36}$$

where c^{max} is the highest propagation velocity to be analyzed. The necessary condition for stability is that the eigenvalues of the matrix in equation 35 is less than or equal to 1.0. This puts an upper limit on $\theta(k_x,k_y,k_z)$,

$$\theta(k_x,k_y,k_z) \le 2. \tag{37}$$

Equation 37 must be valid for all wavenumbers up to the Nyquist wavenumber. The maximum value of the wavenumber response for the staggered-difference operators is of importance for equation 37. This maximum is at the Nyquist wavenumber, which can be deduced from equation 30:

$$\begin{aligned} \partial_{k_x} D_x^+(k_x) &= 0, \\ \partial_{k_x}^2 D_x^+(k_x) &< 0, \end{aligned} \tag{38}$$

for $k_x = \pi/\Delta x$. Therefore, I define

$$\begin{aligned} C_x(L_x) &= \sum_{l_x=1}^{L_x} \alpha_x(l_x)(-1)^{(l_x-1)}, \\ C_y(L_y) &= \sum_{l_y=1}^{L_y} \alpha_y(l_y)(-1)^{(l_y-1)}, \\ C_z(L_z) &= \sum_{l_z=1}^{L_z} \alpha_z(l_z)(-1)^{(l_z-1)}, \end{aligned} \tag{39}$$

and

$$D_x^{\max} = \frac{2}{\Delta x} C_x(L_x),$$

$$D_y^{\max} = \frac{2}{\Delta y} C_y(L_y),$$

$$D_z^{\max} = \frac{2}{\Delta z} C_z(L_z). \quad (40)$$

The resulting stability criterion is

$$\frac{1}{2} c^{\max} \Delta t \sqrt{(D_x^{\max})^2 + (D_y^{\max})^2 + (D_z^{\max})^2} \le 1. \quad (41)$$

Two well-known cases are the CFL limit for an FDTD scheme, second order in space and based on Taylor operators, and the Fourier limit for the pseudospectral method. For simplicity, I assume that all spatial step lengths are equal.

For a second-order scheme with Taylor operators, all operator half-lengths equal 1, $L_i = 1$, and all operator coefficients equal 1.0, $\alpha_i(1) = 1.0$. This gives $C_i(1) = 1.0$ from equation 39 and $D_i^{\max} = 2/\Delta x$ from equation 40. Equation 41 gives

$$c^{\max} \Delta t \frac{1}{\Delta x} \sqrt{3} \le 1, \quad (42)$$

which is the CFL limit.

A pseudospectral scheme is exact up to the Nyquist wavenumber; thus, $D_i^{\max} = \pi/\Delta x$ and equation 41 give the Fourier limit

$$c^{\max} \Delta t \frac{1}{\Delta x} \frac{\pi}{2} \sqrt{3} \le 1. \quad (43)$$

Operators that are fourth order or higher allow time steps that are larger than the Fourier limit in equation 43 but smaller than the limit for the second-order Taylor operator in equation 42. By comparing a Taylor operator to a given order with an optimized operator to the same order, I note that the optimized operator will require a somewhat smaller time step if the spatial step lengths are kept the same. This can be verified by using coefficients from Tables 1 and 2 in equations 39–41. In the case of a sixth-order operator, the Taylor operator time step can be a factor of 1.04 larger than the time step for an optimized operator. However, the optimized operator has better dispersion properties than the Taylor operator; therefore, my spatial sampling can be a factor of 1.57 coarser with an optimized operator. This translates directly to a coarser time step with the same factor and this outweighs the previous factor of 1.04. The net result is that the time step can be increased with a factor of approximately 1.5 for this example.

Boundary conditions

The air-water interface requires special care for a scheme intended for modeling marine CSEM surveys. The remaining five sides of the grid are assumed to be absorbing or transparent. The main issue here is to avoid undesired reflections from the sides that interfere with the solution. This can be achieved with PML-based implementation (Kosloff and Kosloff, 1986; Berenger, 1994) or with absorbing boundaries as given by Cerjan et al. (1985). The last method is used for this scheme.

The air-water interface is implemented at the "first" node in depth, $k = 1$, where k is the depth or z-axis index. However, it is clear from equations 26 and 27 that the horizontal, electric, and magnetic field components are differentiated in the depth direction. This means the horizontal, electric, and magnetic fields are required in a buffer above the first node, $k = 1$. The field components available at $k = 1$ are E_x, E_y, and H_z. A second-order scheme with $L_z = 1$ requires H_x and H_y above $k = 1$ — more precisely at $K = 0$, where $K = k + \frac{1}{2}$ is defined in equation 24. This is because the $\partial_z^- H_x$ and $\partial_z^- H_y$ operations are performed in equation 27. The $\partial_z^+ E_x$ and $\partial_z^+ E_y$ operations in equation 26 do not require the field at ghost nodes above $k = 1$ for $L_z = 1$. However, for $L_z > 1$ both electric and magnetic fields are required above $k = 1$. The implementation of the air-water interface for a 3D FDTD scheme is discussed in Wang and Hohmann (1993). They give a method for obtaining the horizontal magnetic fields at $K = 0$. The underlying assumption is that under the quasi-static assumption we have

$$\nabla \times \boldsymbol{H}(\boldsymbol{x},t) = 0 \quad (44)$$

and

$$\nabla^2 \boldsymbol{H}(\boldsymbol{x},t) = 0 \quad (45)$$

in the air.

Equation 44 is transformed to the spatial wavenumber domain. This gives relations so the horizontal magnetic fields can be expressed as a function of the vertical magnetic field

$$H_x(k_x,k_y,z=0) = -\frac{ik_x}{\sqrt{k_x^2+k_y^2}} e^{-ik_x\frac{\Delta x}{2}} H_z(k_x,k_y,z=0),$$

$$H_y(k_x,k_y,z=0) = -\frac{ik_y}{\sqrt{k_x^2+k_y^2}} e^{-ik_y\frac{\Delta y}{2}} H_z(k_x,k_y,z=0), \quad (46)$$

where the dispersion relation $k_z^2 = -(k_x^2 + k_y^2)$ is obtained from equation 45. Equation 46 has phase-shift terms $e^{-ik_x\frac{\Delta x}{2}}$ and $e^{-ik_y\frac{\Delta y}{2}}$ that compensate for the difference in horizontal staggering of the vertical and horizontal magnetic fields.

Equation 45 implies that the magnetic fields can be extrapolated vertically in the wavenumber domain by

$$H_x\left(k_x,k_y,z=-\frac{\Delta z}{2}\right) = e^{-\sqrt{k_x^2+k_y^2}\frac{\Delta z}{2}} H_x(k_x,k_y,z=0),$$

$$H_y\left(k_x,k_y,z=-\frac{\Delta z}{2}\right) = e^{-\sqrt{k_x^2+k_y^2}\frac{\Delta z}{2}} H_y(k_x,k_y,z=0). \quad (47)$$

Extrapolation to ghost nodes above $K = 0$ — that is, for $K < 0$ — can be performed by repeated application of equation 47 with a depth step equal to Δz:

$$H_x\left(k_x,k_y,z=-\left(m+\frac{1}{2}\right)\Delta z\right) = e^{-\sqrt{k_x^2+k_y^2}m\Delta z} H_x\left(k_x,k_y,z=-\frac{\Delta z}{2}\right),$$

$$H_y\left(k_x,k_y,z=-\left(m+\frac{1}{2}\right)\Delta z\right) = e^{-\sqrt{k_x^2+k_y^2}m\Delta z}H_y\left(k_x,k_y,z=-\frac{\Delta z}{2}\right). \quad (48)$$

All that is required after this is a transform back to the space domain. However, this is a scheme using high-order operators so the electric field must also be extrapolated into the air if $L_z > 1$. The quasi-static approximation for the electric field is (Oristaglio and Hohmann, 1984),

$$\nabla^2 \boldsymbol{E}(\boldsymbol{x},t) = 0. \quad (49)$$

Thus, the horizontal electric field components in the air layer can be obtained by a transform to the wavenumber domain and extrapolation to any node level above $z = 0$ by

$$E_x(k_x,k_y,z=-m\Delta z) = e^{-\sqrt{k_x^2+k_y^2}m\Delta z}E_x(k_x,k_y,z=0),$$
$$E_y(k_x,k_y,z=-m\Delta z) = e^{-\sqrt{k_x^2+k_y^2}m\Delta z}E_y(k_x,k_y,z=0), \quad (50)$$

before a transform back to the space domain.

An implementation of the airwave also requires that the conductivity at the air-water interface be handled properly. The conductivity in air is set to zero. Thus, at the node in depth where the air-water interface is implemented, I assume the effective conductivity is half that of the water layer.

Simulation times

The transform from the fictitious wave domain to the diffusive frequency domain contains an exponential decay factor, as can be seen in equation 17. Thus, early arrivals are weighted heavily compared to late arrivals. This gives an upper limit on how many time steps (N_t) are required for the simulation in the fictitious wave domain. The time integration in equation 17 can be performed while the FDTD simulation is running. This time integration and, hence, the FDTD simulation can be stopped when the frequency-domain result does not change with increasing time at the maximum source-receiver offset.

A safe estimate of this limit $T^{\max}$ is given by the time it takes for the signal that propagates in the seawater over a distance that represents the largest source-receiver separation $R^{\max}$. This gives an overestimate of the required simulation time $T^{\max}$ because in practice the time it takes for the signal to propagate as a refracted event just below the seabed from the source to a large offset receiver is critical. This event arrives earlier than the water layer event because the propagation velocity is much larger.

An alternative approach is to perform an analysis in the diffusive frequency domain and determine the consequences in the fictitious wave domain. The average conductivity of seawater is 3.2 S/m. A fair estimate of the overburden conductivity is 1.0 S/m. If these values are used for a half-space model, I find that the amplitude of the refracted field at the seabed is 10^3 times larger than the direct field in the water layer at an 8-km source-receiver separation. Thus, the direct wave is negligible at this offset. The implication for the fictitious wave-domain simulation is that if I let the simulation time be sufficiently large to allow the direct wave to reach a distance from the source that is 8 km, then all important contributions should be present in the fictitious wave-domain field because later arrivals in this domain will not survive the transformation to the diffusive frequency domain.

However, for the sake of the arguments to follow, I use the safe or overestimated value for $T^{\max}$, assuming it to be the traveltime for the field propagating from the source to the receiver in the water layer. Equation 14 is a wave equation. For the following derivation and for simplicity, I assume an isotropic conductivity model. The propagation velocity $c(\boldsymbol{x})$ is then given by equation 15. For further simplification, I assume that all spatial step lengths are equal. Then from equation 41,

$$\Delta t = \kappa\frac{\Delta x}{c^{\max}}, \quad (51)$$

where κ is given by the properties of the difference operator so that the calculation is stable. Further, I assume the two horizontal dimensions of the model are of a similar size. Hence, the number of nodes in the y-direction (N_y) is close to the number of nodes in the x-direction (N_x). It is then reasonable to assume

$$R^{\max} = SN_x\Delta x, \quad (52)$$

where S is between 0.5 and 1.0. For the moment, I neglect the duration of the signal in the fictitious wave domain. This is discussed at the end of this section. The simulation time is then

$$T^{\max} = \frac{R^{\max}}{c^{\min}} = \frac{SN_x\Delta x}{c^{\min}}. \quad (53)$$

The number of time steps is

$$N_t = \frac{T^{\max}}{\Delta t} = \frac{SN_x}{\kappa}\frac{c^{\max}}{c^{\min}} = \frac{SN_x}{\kappa}\sqrt{\frac{\sigma^{\max}}{\sigma^{\min}}}. \quad (54)$$

Thus, N_t is independent of the choice of ω_0 but dependent on the square root of the ratio between highest and lowest conductivity. This can be explained as follows: If ω_0 increases then the highest propagation velocity increases with a factor of $\sqrt{\omega_0}$ and the stability criterion dictates a reduction in Δt with a factor of $1/\sqrt{\omega_0}$. At the same time, the lowest propagation velocity increases with a factor of $\sqrt{\omega_0}$. This implies that the simulation time can be reduced by a factor of $1/\sqrt{\omega_0}$. These two effects cancel each other out in equation 54.

The number of time steps for this method can be compared with the number of time steps required for the diffuse scheme described by Wang and Hohmann (1993). I assume the grid sizes and step lengths are equal. The number of floating-point operations required to calculate the curls of the magnetic and electric fields are then the same if the difference operators are the same. For practical simulations in the fictitious time domain, I arbitrarily choose $f_0 = 1.0$ Hz and $\omega_0 = 2\pi f_0$. I assume that all spatial step lengths are 100 m. The minimum conductivity is set to 0.02 S/m and the maximum conductivity to 3.2 S/m. The lowest and highest propagation velocities given by equation 15 are 1767 m/s and 22,361 m/s, respectively. If I assume that my highest offset is 10 km, then the signal in the seawater will need 5.7 s to reach this offset at 1767 m/s. I add 1.0 s in simulation time to include the duration of the source time function. If I assume a standard second-order scheme in space, then $\kappa = 1/\sqrt{3}$ in equation 51. The stability criterion gives a time step of 2.58 ms. The required number of time steps for the fictitious time-domain simulation is 2597.

Wang and Hohmann (1993) give a method for varying the time step in their equation 21:

$$\Delta t_{\max} = \alpha \sqrt{\frac{\mu \sigma^{\min} t}{6}} \Delta x, \tag{55}$$

where α ranges from 0.1 to 0.2 depending on the accuracy required. In the example to follow, I use $\alpha = 0.15$. The typical maximum offset in a marine CSEM survey is 10 km. The duration of the impulse response in the diffusive domain at a 10-km offset will be approximately 200 s. Using equation 55, I find that 29,139 time steps are required. With these numbers, I find the simulation via the fictitious wave domain is at least ten times more efficient than the diffusive simulation with variable time steps. However, Maaø (2007) finds accuracy problems at source-receiver offsets of 10 km with a displacement current of the magnitude proposed by Wang and Hohmann (1993). This indicates that the value of α in equation 55 should be reduced further. Maaø (2007) reports that his method is 40 times more effective than a diffusive simulation. This comparison is with a scheme of the type proposed by Wang and Hohmann (1993) but with an assumed fixed time step for the diffusive simulation.

The scheme proposed here will be at least as effective as the complex frequency scheme proposed in Maaø (2007). The reason is that the complex frequency scheme is partly diffusive and has a diffusive tail that arrives after the wavelike component. This contribution must be included in the simulated time-domain data before the transformation to the diffusive domain and will in principle increase the total simulation time compared to a nondiffusive scheme. This diffusive tail is not present in a scheme based on the correspondence principle. However, as shown in Appendix A, by a proper choice of the complex frequency parameter α, the complex frequency method and the method presented here, based on the correspondence principle, can be effectively the same.

The order of the operator or the operator half-length also plays a key role in determining computational time. Equation 53 is not complete. It is necessary that the electromagnetic fields are causal and that the integration in equation 17 covers the duration of an arrival. A source pulse used in a finite-difference scheme must be properly band-limited to avoid dispersion. If the source time function is a Gaussian,

$$\Gamma(t') = \sqrt{\frac{\beta}{\pi}} e^{-\beta(t' - t_0)^2}, \tag{56}$$

or a time derivative of the Gaussian, then the duration of the pulse typically will be $2t_0$. However, t_0 can be moved to earlier times if the frequency content is increased. The frequency content is controlled by the parameter β. If I assume the step lengths to be used for the calculation already given, then the maximum allowed frequency would depend on the operator half-length through the value of G_{lim} in Table 1,

$$f_{\max} = \frac{c_{\min}}{G_{\lim} \Delta x}. \tag{57}$$

The source pulse now can be fixed by using equation C-8, $\beta \approx \pi f_{\max}^2$, and equation C-9, $t_0 \approx \frac{\pi}{f_{\max}}$. The total required simulation time T^{max} in equation 53 is modified as $T^{\max} \rightarrow T^{\max} + 2t_0$. Hence, the total simulation time depends on the operator half-length. The time step is given by the stability condition in equation 41, which implies that the time step also depends on the operator half-length. The number of numerical operations required to solve the Maxwell equations for one time step increases linearly with the operator half-length. However, the rate of GFLOPs also depends on the operator half-length. Normally, the GFLOP rate or numerical efficiency also increases with operator half-length over some interval. The reason is that differentiation with a high-order operator has a higher degree of re-use of data fetched from the main memory compared to differentiation with a low-order operator. The computer architecture and in particular the size of the secondary cache plays an important role here. It can also be the case that calculation with operators that are too long saturates the secondary cache so that numerical efficiency drops. The above scheme has been tested on several architectures and the conclusion is that simulation with operator half-lengths of 2 and 3 are the most numerically effective. A second-order scheme $L_i = 1$ is approximately as efficient as an eighth-order scheme $L_i = 4$ if the accuracy is required to be the same.

RESULTS

The choice of the scale parameter ω_0 is in principle arbitrary. In the examples to follow, I use $\omega_0 = 2\pi f_0$ with $f_0 = 1$ Hz. Typical propagation velocities in the water layer are then 1700–1800 m/s. Typical propagation velocities for a relatively conductive formation are 3000–6000 m/s. The propagation velocity in a 50 Ωm resistor is approximately 22,500 m/s.

All examples are with step lengths of 100 m. This is sufficient for the examples given here. Davydycheva et al. (2003) give a method to scale conductivity on a finer grid up to a coarser grid. This method also gives good results for the present scheme, especially for thin resistors that can be mapped to a coarser grid while preserving the transverse resistance. An alternative upscale procedure is described by Commer and Newman (2006).

All examples are done with a transmitter time function in the fictitious wave domain that behaves as the first derivative of a Gaussian,

$$J_n'^T(t') = -2\beta(t' - t_0)\sqrt{\frac{\beta}{\pi}} e^{-\beta(t' - t_0)^2}. \tag{58}$$

There is great freedom in choosing the form of the transmitter time function and its frequency content in the fictitious wave domain as long as it is causal or sufficiently small at the initial time. The advantage of using the first derivative of a Gaussian is most apparent if an impulse response is required in the diffusive time domain. The impulse response in the diffusive time domain has a DC contribution not equal to zero. Thus, $J_n^T(\omega = 0) \neq 0$ is required in equation 20 to build the proper spectrum for equation 21. The zero-frequency situation does not require a special analysis or implementation if the transmitter time function in the fictitious wave domain is the first derivative of a Gaussian, as can be seen from equation C-11. In this case, the ω term in the denominator of equation 19 is canceled in the transform. There is an advantage in terms of reduced CPU time to run with a transmitter waveform in the fictitious wave domain that has high frequency content, as already mentioned.

The maximum allowed frequency is given by the grid lengths and the dispersion properties of the derivative operators. The time t_0 in equation 58 can be moved to earlier times because the frequency content is increased and the waveform is sharpened and can still give a time function that is approximately causal. If the maximum frequency f_{max} is given from the dispersion analysis, I use $\beta = \pi f_{max}^2$ and $t_0 = \pi / f_{max}$.

The fictitious wave domain

The first example is of the electromagnetic field in the fictitious wave domain. The resistivity (conductivity) model is shown in Figure 1. This example is performed with a grid spacing of 20 m and a maximum source frequency of 25 Hz. The operator half-length is four for all three spatial directions.

This problem could have been solved equally well with a 100-m grid spacing and a maximum frequency of 5 Hz. The high-frequency content and dense sampling is chosen for illustration purposes: It helps separate events on the snapshots shown in Figures 2 and 3. This is a shallow-water case with a water depth of 200 m. The area above the red line in Figures 2 and 3 is air. The electromagnetic field is extrapolated into this domain of the model by equations 46–50. The blue line indicates the seabed, the green line indicates the resistor, and the black line shows the boundary to the lower half-space. The snapshots in Figures 2 and 3 are for the inline electric field in the source plane. These are snapshots of the inline electric field still in the fictitious wave domain and prior to the transform to the diffusive frequency domain.

The amplitudes in Figure 2 are scaled up so that the airwave is visible. The airwave is the horizontal event at a depth of 150 m. The arrows indicate the propagation direction. The airwave amplitude is not large compared to other events in the fictitious wave domain but it could contribute significantly to the field amplitudes in the diffusive domain resulting from its early arrival. It is apparent from the inspection of snapshots for times neighboring the time of the snapshot in Figure 2 that the airwave is the first arrival at the seabed above a source-receiver separation of 1 km.

The second arrival at a 1-km offset is the wave refracted along the seabed. This is the strongest event at 1 km. It also dominates the diffuse contribution at this offset. However, the second arrival at a 2-km source-receiver separation is the first water-bottom multiple of the airwave. The contribution of the airwave in the diffusive domain increases from this offset and outward because the time series is weighted with the term $e^{-\sqrt{\omega\omega_0}t}$, as can be seen in equation 17. Late arrivals in the fictitious wave domain are exponentially damped compared to early arrivals when diffusive field contributions are extracted.

Figure 3 displays the inline electric field at a later stage. The amplitude scaling is reduced compared to Figure 2. The contribution from the resistor is clearly visible and the propagation direction is illustrated with the black arrow. The contribution from the resistor will be the third arrival for source-receiver separations above 2.5 km except for some high-order water-bottom multiples of the airwave.

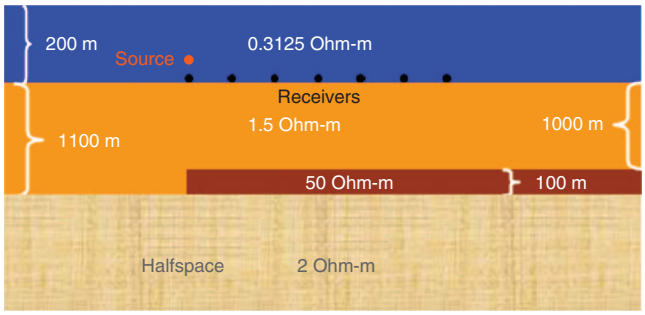

Figure 1. The cross-section of the 3D resistivity (conductivity) model used for the snapshot examples.

The contribution from the resistor becomes important in the diffusive domain because it arrives relatively early at large offsets in the fictitious wave domain and has high amplitude.

The transform in equation 17 that takes the data from the fictitious wave domain to the diffusive domain is a temporal transform. It will not affect the propagation paths taken by the field in the fictitious wave domain. Thus, the propagation paths in the fictitious wave domain and the real diffusive domain must be the same. This is also the case for scattering amplitudes. If the medium is inhomogeneous, there will be scattered events. These scattered events can be described by reflection and transmission amplitudes for simple models. The reflection and transmission coefficients must be the same in the fictitious wave domain and in the real diffusive domain. However, the transform in equation 17 puts a strong weight on early arrivals. The early arrivals in the fictitious wave domain at small offsets (less than 1–2 km) in a typical marine CSEM setting are reflections. However, for larger offsets the early arrivals at the seabed are dominated by postcritical events such as refracted and guided waves. This makes sense when comparing to the diffusive fields obtained after the transform from the fictitious wave domain. The early arrivals in the fictitious wave domain have taken a high-velocity path, which equals low conductivity in the fictitious wave domain. Thus, the observed field in the diffusive domain is dominated by the propagation paths that have experienced the least absorption.

It could be inferred that ray tracing is an option for the simulation of the electromagnetic fields in a CSEM survey because the fields

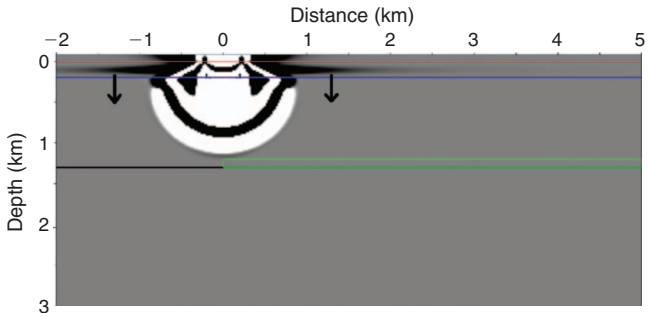

Figure 2. Snapshot of the inline electric field in the source plane at an early time. The blue line indicates the seabed, the green line indicates the resistor, and the black line shows the boundary to the lower half-space. The airwave is the horizontal event at a depth of 150 m. The arrows indicate the propagation direction.

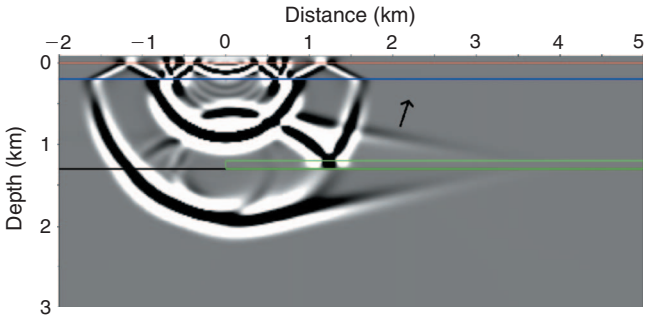

Figure 3. Snapshot of the inline electric field in the source plane at an intermediate time. The blue line indicates the seabed, the green line indicates the resistor, and the black line shows the boundary to the lower half-space. The contribution from the resistor is the dipping event just below the black arrow. The arrow indicates the propagation direction.

can be simulated by a wave equation. Ray tracing is an option in seismic modeling because a significant contribution to the total recorded field is precritical reflections. These are fairly easy to implement numerically. However, as stated above, the parts of the electromagnetic field that are important in a marine CSEM survey are typically postcritical and guided events. These are more cumbersome to implement in a ray-tracing code.

The diffusive frequency domain

Most marine CSEM surveys to date have been performed with a periodic transmitter current. The transmitter waveform typically will concentrate the output energy on a subset of frequencies — normally, three to five frequencies. However, a larger span of frequencies usually is analyzed in the survey design; therefore, one of the advantages of the scheme discussed here is that a multitude of frequencies can be extracted from a single modeling run.

I use a deep-water model and a shallow-water model to demonstrate the performance of the method for calculating diffusive fields in the frequency domain. The FDTD fields are compared to reference fields calculated with a plane-layer method (Løseth and Ursin, 2007). The deep-water model is shown in Figure 4. The water depth is 3050 m. The resistor is buried 1000 m below the seabed and has a thickness of 100 m. The FD grid has a spacing of 100 m in all spatial directions and the operator half-lengths are three. The source maximum frequency in the fictitious wave domain is 3 Hz. The frequencies 0.25, 0.75, and 1.25 Hz are extracted from the FDTD calculation. The amplitude and phase curves of the inline electric field are shown in Figure 5. The black curves represent the plane-layer method and the green curves represent the FDTD method after the transforms in equations 17 and 19 are followed by the source deconvolution in equation 20. The normalized amplitude ratios between the two methods stay within 1.0 ± 0.001 for 0.25 Hz and 1.0 ± 0.008 for 1.25 Hz. The discrepancy increases moderately with frequency but good results can be obtained for all frequencies normally used in marine CSEM experiments. The phase difference stays within 1 degree at 0.25 Hz and within 4 degrees at 1.25 Hz. A phase difference $\Delta\phi$ (in radians) can be equated with an angular frequency $2\pi f$ times a time difference $\Delta\tau$ so that $\Delta\phi = 2\pi f \Delta\tau$. If this is done for the phase curves shown in Figure 5, then this time difference is approximately 10 ms for all frequencies. The typical sampling interval used for CSEM receivers today is 20 ms so this difference is approximately half the sampling interval.

The shallow-water model is shown in Figure 6. The step lengths, operator half-lengths, and transmitter maximum frequency are as for the deep-water case. The amplitude and phase curves for the inline electric field are shown in Figure 7. The black curves represent the plane-layer method and the green curves represent the FDTD method. The normalized amplitude ratios between the two methods stay within 1.0 ± 0.03 for all frequencies. The phase difference stays within 0.2 degrees for 0.25 Hz and within 1 degree at 1.25 Hz. Thus, if I take the plane-layer modeling to give the ground truth, when I compare the deep-water case with the shallow-water case, I find that amplitudes are modeled more correctly in the deep-water case and the phase responses are modeled more accurately in the shallow-water case. I have not identified the source of this difference. I find the discrepancies in either case to be sufficiently small to give reliable results for simulation of real data.

A real data case is shown in Figure 8. The observed data is from a recent survey over the Troll West Gas Province described in Gabrielsen et al. (2009). The chosen receiver is from the "2D monitoring line" described there and is situated close to the edge of the reservoir. The negative offsets in Figure 8 are for the source outside the reservoir and the positive offsets are for the source above the reservoir.

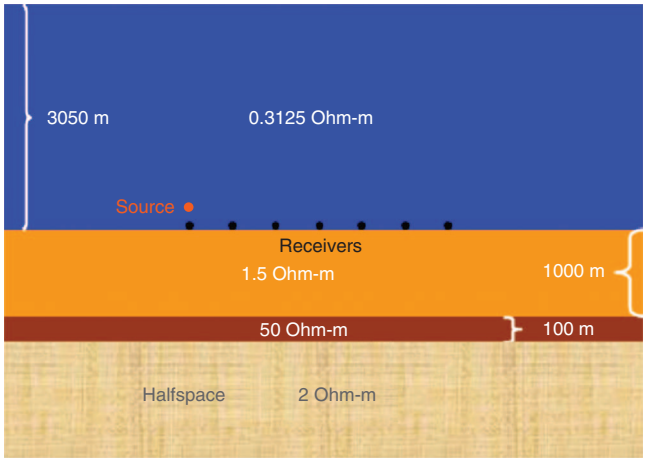

Figure 4. The cross-section of the deep-water 3D resistivity (conductivity) model used for comparison with the plane-layer method.

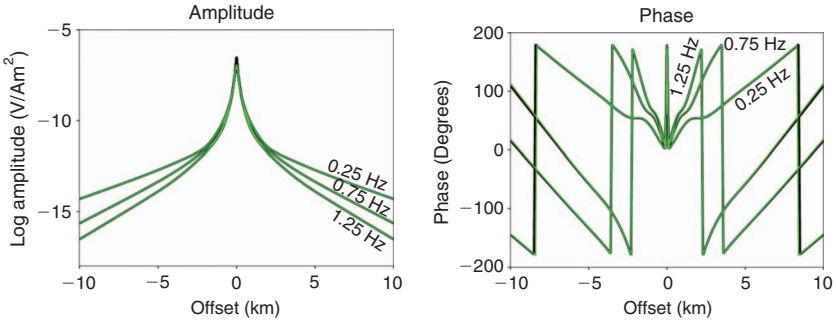

Figure 5. Inline electric field for 0.25, 0.75, and 1.25 Hz for the deep-water case. The black lines are for plane-layer modeling. The green lines are for FDTD modeling.

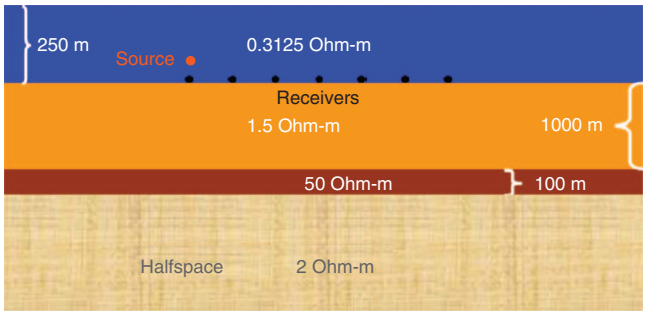

Figure 6. The cross-section of the shallow-water 3D resistivity (conductivity) model used for comparison to the plane-layer method.

Cross-sections of the horizontal and vertical resistivity models are shown in Figure 9. The position of the receiver is at 14.5 km, which is approximately 1.5 km outside the reservoir on the left side. The water depth is approximately 330 m; therefore, there is a substantial airwave component in the observed data. The horizontal and vertical conductivity models used for the simulation were derived from full waveform inversion of the complete line. The inversion method used was an in-house 2.5D scheme with a different modeling algorithm than the one discussed here. The retrieved conductivity models have no variations normal to the towline direction. Models with 3D variations cannot be obtained from a single survey line but require data acquired on a surface grid. This was not available here.

The resistivity in the water layer was 0.29 Ωm. The horizontal resistivity varied from 1.2 Ωm in the shallow part of the model to 1.5–1.8 Ωm below 1800 m with a slight increase in resistivity along the towline (increasing x-coordinate). The vertical resistivity has a value of 3.5–3.8 Ωm from the mud line down to 500 m. From 500 m and down to the top reservoir at 1300 m, the vertical resistivity is 2.2 Ωm. Below 1800 m, the vertical resistivity is 3.0–3.5 Ωm with an increase along the towline. The simulation was performed with grid lengths of 100 m in the two horizontal directions and 50 m in the depth direction. Fourth-order optimized derivative operators were used for all three spatial dimensions. The fit between the observed and synthetic data is in general very good for both amplitude and phase. The remaining misfit can very well be caused by the fact that we do not know the subsurface with sufficient accuracy.

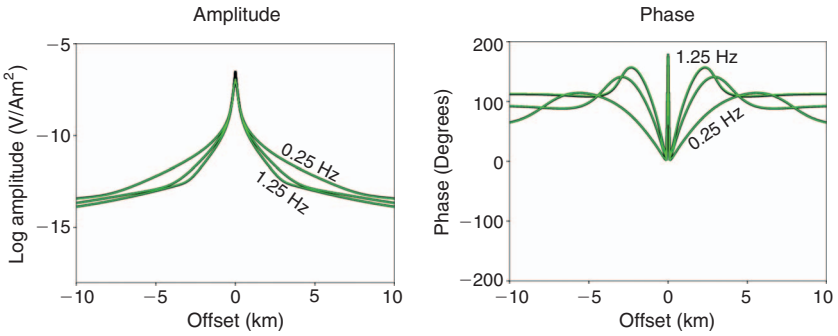

Figure 7. Inline electric field for 0.25, 0.75, and 1.25 Hz for the shallow-water case. The black lines are for plane-layer modeling. The green lines are for FDTD modeling.

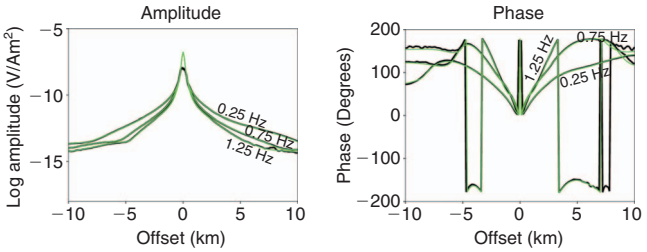

Figure 8. Comparison of real and synthetic inline diffusive electric fields for a receiver over the Troll West Gas Province. The real data are in black and the synthetic data are in green. The frequencies are 0.25, 0.75, and 1.25 Hz.

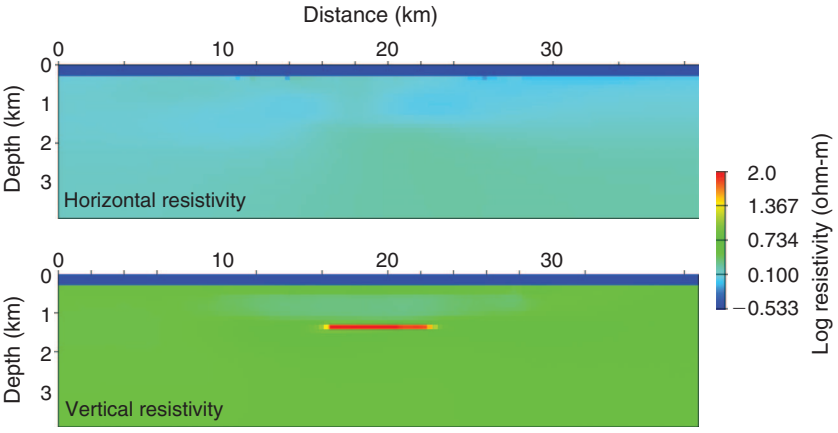

Figure 9. Cross-sections of horizontal and vertical resistivities used for the simulation of+ synthetic data in Figure 8.

The diffusive time domain

The diffusive time-domain response can be calculated if the diffusive frequency-domain response is available over a sufficiently large frequency range. The calculation of the diffusive time-domain response does not increase the simulation time in the fictitious wave domain except for the calculation of frequency responses in equation 17 and a final FFT that takes the recorded data from the diffusive frequency domain to the diffusive time domain.

The whole-space solution of the impulse response of the electric field can be found by a time differentiation of equation 2.50 in Ward and Hohmann (1987). Figure 10 shows the inline electric field at an offset of 5000 m in a 1 Ωm whole-space as the black curve. The green curve is the result of an FDTD simulation in the fictitious wave domain. The wave-domain inline electric field is transformed according to equations 17, 19, and 20, followed by equation 21. The step lengths used were 100 m, the operator half-lengths were all equal to two, and the maximum transmitter frequency was 1 Hz.

I have also extracted diffusive time-domain solutions from the simulations described above for the models in Figures 4 and 6. The comparison is with the plane-layer method described in Løseth and Ursin (2007). For this method, a sufficiently large frequency spectrum was calculated and the spectrum was transformed to the time domain to give the impulse response. The deep-water response of the inline electric field at a source-receiver separation of 5000 m is shown in Figure 11 and the shallow-water response of the inline electric field at a source-receiver separation of 9000 m is shown in Figure 12. The fit for the deep-water case is good for the whole time sequence.

The main contribution at 5000 m is the response from the resistor. There is a small discrepancy between the two methods at times earlier than 0.03 s for the shallow-water case but the first peak, which corresponds to the air wave, and the second peak, which is dominated by the resistor contribution, are very close in amplitude for both methods. The two most challenging areas for extracting the time-domain impulse response in the diffusive domain from the FDTD simulations in

the fictitious wave domain are the near-field, where the contributions from high frequencies dominate, and very large offsets in deep water, where the duration of the signal is large. The long duration of the signal dictates a very fine frequency sampling to avoid wrap-around effects in the transform from the diffusive frequency domain to the diffusive time domain.

Back to the fictitious wave domain

The area of application for modeling tools based on the correspondence principle increases if it is possible to transform data from the diffusive domain to the fictitious wave domain. This opens up the possibility of performing adjoint state reconstruction of a field from a measured boundary condition, a key factor in calculating the gradient with respect to model parameters (Tarantola, 1984). There is a large class of inverse methods that requires the gradient from the present iteration plus potential gradients from previous iterations to perform the model update, among which are steepest descent, conjugate gradient, and BFGS types of schemes. It is already well established that the transform from the diffusive frequency domain to the fictitious wave domain is ill-posed. Equation C-11 combined with equation C-14 shows there is a nonuniqueness problem related to this transform. From the combination of these two equations, it is clear that an infinite multitude of source waveforms in the fictitious wave domain give the desired solution in the diffusive frequency domain. The nonuniqueness is not necessarily a disadvantage. It gives a large degree of freedom in postulating the source waveform in the fictitious wave domain. This postulated waveform can be estimated by an inverse procedure. This topic is also covered by Støren et al. (2008) for the complex frequency method of Maaø (2007).

Assuming that $E_n^B(\boldsymbol{x}_r,t)$ is a boundary condition for the diffusive field, the adjoint state is according to Tarantola (1984),

$$E_k(\boldsymbol{x},t) = \int_0^T d\tau \int dS(\boldsymbol{x}_r) G_{kn}^{EJ}(\boldsymbol{x},\tau|\boldsymbol{x}_r,t) E_n^B(\boldsymbol{x}_r,\tau)$$

$$= \int_0^T d\tau \int dS(\boldsymbol{x}_r) \tilde{G}_{kn}^{EJ}(\boldsymbol{x},t|\boldsymbol{x}_r,\tau) E_n^B(\boldsymbol{x}_r,\tau), \quad (59)$$

where $\tilde{G}_{kn}^{EJ}(\boldsymbol{x},t|\boldsymbol{x}_r,\tau)$ is the adjoint state Green's function and $dS(\boldsymbol{x}_r)$ is a surface integral element over the receiver domain. The frequency-domain representation is

$$E_k(\boldsymbol{x},\omega) = \int dS(\boldsymbol{x}_r) \tilde{G}_{kn}^{EJ}(\boldsymbol{x},\omega|\boldsymbol{x}_r) E_n^B(\boldsymbol{x}_r,\omega), \quad (60)$$

where the tilde indicates a complex conjugate. If it is possible to obtain a boundary condition $E_n'^B(\boldsymbol{x}_r,t')$ in the fictitious wave domain that fulfills

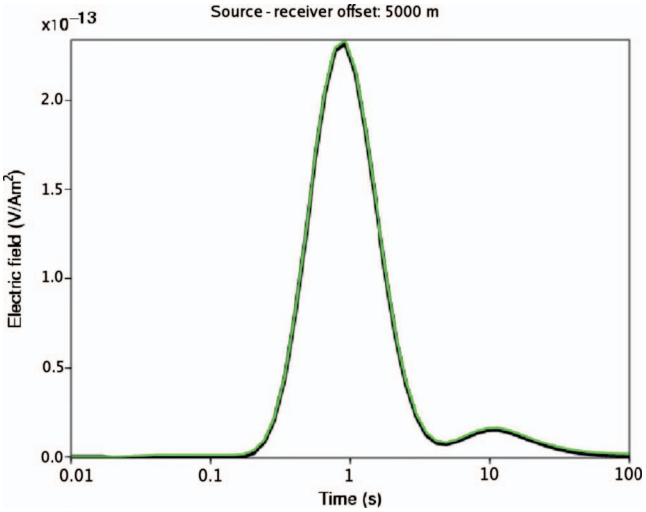

Figure 11. Comparison of the inline diffusive electric field in the deep-water model at a source-receiver offset of 5000 m. The plane-layer result is in black. The FDTD result is in green.

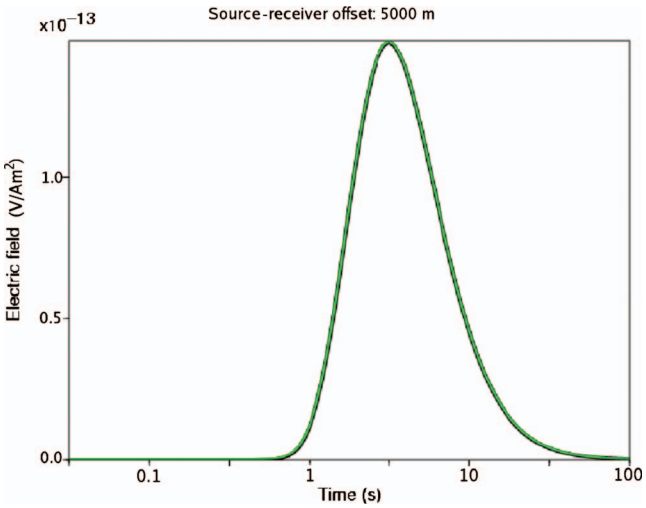

Figure 10. Comparison of the inline diffusive electric field in a whole-space model at a source-receiver offset of 5000 m. The analytic result is in black. The FDTD result is in green.

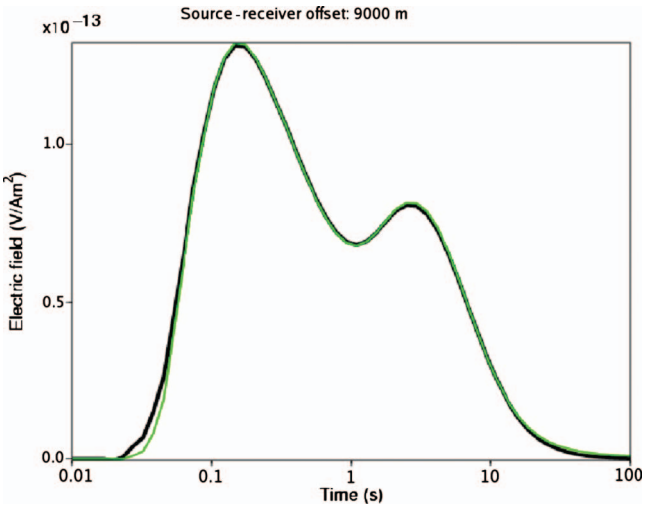

Figure 12. Comparison of the inline diffusive electric field in the shallow-water model at a source-receiver offset of 9000 m. The plane-layer result is in black. The FDTD result is in green.

$$E_n^B(\boldsymbol{x}_r,\omega) = \int_0^T dt' E_n'^B(\boldsymbol{x},t') e^{-\sqrt{\omega\omega_0}t'} e^{i\sqrt{\omega\omega_0}t'}, \quad (61)$$

then the adjoint state $E_k'(\boldsymbol{x},t')$ in this domain is

$$E_k'(\boldsymbol{x},t') = \int_0^T d\tau' \int dS(\boldsymbol{x}_r) \tilde{G}_{kn}'^{EJ}(\boldsymbol{x},t'|\boldsymbol{x}_r,\tau') E_n'^B(\boldsymbol{x}_r,\tau'), \quad (62)$$

where $\tilde{G}_{kn}'^{EJ}(\boldsymbol{x},t'|\boldsymbol{x}_r,\tau')$ is the adjoint state Green's function in the fictitious wave domain. The relation between this Green's function and the adjoint state Green's function in the diffusive domain can be derived from equations 17–20, assuming that $J_n'^T(t') = \delta(t'-\tau')$ and

$$\int_0^T dt' \tilde{G}_{kn}'^{EJ}(\boldsymbol{x},t'|\boldsymbol{x}_r,\tau') e^{-\sqrt{\omega\omega_0}t'} e^{i\sqrt{\omega\omega_0}t'} = \sqrt{\frac{2\omega_0}{i\omega}} \tilde{G}_{kn}^{EJ}(\boldsymbol{x},\omega|\boldsymbol{x}_r) e^{-\sqrt{\omega\omega_0}\tau'} e^{i\sqrt{\omega\omega_0}\tau'}. \quad (63)$$

The transform of the field in equation 62 gives the field $\bar{E}_k(\boldsymbol{x},\omega)$, which is related to the desired field in equation 60 by

$$\begin{aligned}\bar{E}_k(\boldsymbol{x},\omega) &= \int_0^T dt' E_k'(\boldsymbol{x},t') e^{-\sqrt{\omega\omega_0}t'} e^{i\sqrt{\omega\omega_0}t'} \\ &= \int_0^T dt' \int_0^T d\tau' \int dS(\mathbf{x}_r) \tilde{G}_{kn}'^{EJ}(\boldsymbol{x},t'|\boldsymbol{x}_r,\tau') \\ &\quad \times E_n'^B(\boldsymbol{x}_r,\tau') e^{-\sqrt{\omega\omega_0}t'} e^{i\sqrt{\omega\omega_0}t'} \\ &= \sqrt{\frac{2\omega_0}{i\omega}} \int dS(\boldsymbol{x}_r) \tilde{G}_{kn}^{EJ}(\boldsymbol{x},\omega|\boldsymbol{x}_r) E_n^B(\boldsymbol{x}_r,\omega) \\ &= \sqrt{\frac{2\omega_0}{i\omega}} E_k(\boldsymbol{x},\omega). \end{aligned} \quad (64)$$

As I have already noted, the transform from the diffusive frequency domain to the fictitious wave domain is nonunique. This gives a large degree of freedom in choosing the representation of the time function in the fictitious wave domain. I propose to use as base functions the second derivative of the Gaussian as given in equation 56:

$$\Gamma(t'-\tau_m) = \sqrt{\frac{\beta_m}{\pi}} e^{-\beta_m (t'-\tau_m)^2}, \quad (65)$$

with a fixed choice of β_m to ensure causality,

$$\beta_m = \frac{\pi^3}{\tau_m^2}, \quad (66)$$

which results from $f_{\max} = \frac{\pi}{\tau_m}$ and $\beta_m = \pi f_{\max}^2$.

The index m runs over the number of frequencies to fit so that the estimated fictitious wave-domain boundary condition $\hat{E}_n^B(\boldsymbol{x}_r,t')$ becomes

$$\hat{E}_n^B(\boldsymbol{x}_r,t') = \sum_m A_m \partial_{t'}^2 \Gamma(t'-\tau_m). \quad (67)$$

The frequency-domain representation is

$$\hat{E}_n^B(\boldsymbol{x}_r,\omega) = \sum_m A_m 2\omega\omega_0 e^{-\sqrt{\omega\omega_0}\tau_m} e^{i\sqrt{\omega\omega_0}\tau_m} e^{-i\frac{\omega\omega_0\tau_m^2}{2\pi^3}} e^{-i\frac{\pi}{2}}. \quad (68)$$

The above function has $2m$ parameters, A_m and τ_m, that must be estimated. I minimize the functional ϵ, which measures the difference between the observed boundary condition $E_n^B(\boldsymbol{x}_r,\omega)$ and the estimate $\hat{E}_n^B(\boldsymbol{x}_r,\omega)$, in the least-squares sense in

$$\epsilon = \sum_\omega (E_n^B(\boldsymbol{x}_r,\omega) - \hat{E}_n^B(\boldsymbol{x}_r,\omega))^* (E_n^B(\boldsymbol{x}_r,\omega) - \hat{E}_n^B(\boldsymbol{x}_r,\omega)). \quad (69)$$

I have $2m$ observations because I use m frequencies with $E_n^B(\boldsymbol{x}_r,\omega)$ complex. An example of a real data set with three frequencies is shown with black curves in Figure 13. This is the same data set from Troll as shown in Figure 8. The inline electric field is plotted. The field $\hat{E}_x^B(\boldsymbol{x}_r,t')$ resulting from equation 67 is shown in Figure 14. The transformation of $\hat{E}_x^B(\boldsymbol{x}_r,t')$ to the diffusive frequency domain is shown as the green curve in Figure 13. The fit between $E_x^B(\boldsymbol{x}_r,\omega)$ and the estimate $\hat{E}_x^B(\boldsymbol{x}_r,\omega)$ is very good. Figure 14 shows one of an infinite number of valid representations for $\hat{E}_x^B(\boldsymbol{x}_r,t')$. Each trace in Figure 14 is normalized to unity. The true-amplitude variation with source-receiver separation is much larger than what seems apparent in Figure 14.

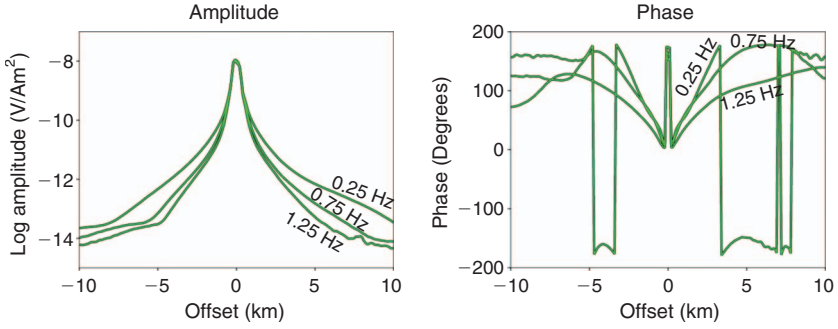

Figure 13. Comparison of an observed inline electric field (black curve) with the result of first obtaining a representation of the same field in the fictitious wave domain and then taking this field back to the diffusive frequency domain (green curve).

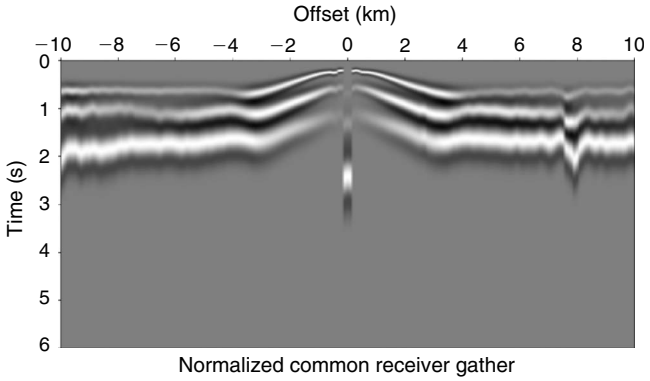

Figure 14. One possible representation in the fictitious wave domain of the observed frequency-domain inline electric field in Figure 13. Each trace is normalized to unity to display the field at large source-receiver offsets.

CONCLUSION

The correspondence principle for wave and diffusion fields can be used to implement numerically highly efficient FDTD schemes to simulate marine CSEM data. The numerical efficiency is resulting from two factors: The first is that a relatively large time step can be taken because a hyperbolic system is solved; the second is that relatively short simulation times can be used because the transform from the fictitious time domain to the diffusive frequency domain quenches late arrivals caused by the exponential decay factor. The method is very well suited for modeling frequency-domain diffusive fields but also time-domain diffusive fields can be recovered. The scheme here is with optimized derivative operators. Second-order to eighth-order operators are implemented for flexibility. For this particular method, I find the choice of fourth-order and sixth-order operators gives the most numerically efficient calculations, but this result depends on computer architecture. An implementation with high-order operators requires that both electric and magnetic fields be extrapolated simultaneously into the air layer to obtain a proper description of the airwave.

A scaling parameter ω_0 is introduced for convenience to simplify dispersion and stability analysis. The diffusive domain Green's tensor is independent of the scaling parameter. I have formulated a stability condition for high-order staggered-derivative operators that is also valid for acoustic and elastic seismic wave propagation.

The bandwidth of the recovered fields in the diffusive domain is independent of the bandwidth of the fields in the fictitious wave domain. The fields in the fictitious wave domain do not represent observable fields but the propagation paths and interaction/reflection amplitudes are not altered by the transform from the fictitious wave domain to the diffusive frequency domain, except for the fact that this transform contains an exponential decay factor that damps down late arrivals in the fictitious wave domain. This fact can be used to estimate the maximum required simulation time in the fictitious wave domain. The simulation can be terminated safely when the direct wave in the water reaches the maximum source-receiver separation.

The propagation paths that contribute most to the diffusive domain fields are the airwave (in shallow water) plus typically postcritical events such as refracted and guided events. The transform from the diffusive frequency domain to fictitious wave domain is an ill-posed problem. The transform is nonunique. There is a multitude of field representations in terms of the waveform in the fictitious wave domain that can give the proper field behavior in the diffusive domain. This gives a large degree of freedom in postulating temporal waveforms for boundary conditions in the fictitious wave domain that reproduce correct diffusive frequency-domain fields.

ACKNOWLEDGMENTS

I thank Electromagnetic Geoservices (EMGS ASA) for allowing the publication of this work. I also thank my colleagues Kristian Rymann Hansen, Frank Maaø, Friedrich Roth, and Daniil Shantsev for discussions. I thank Mark Everett and two anonymous reviewers for their helpful comments.

APPENDIX A

THE COMPLEX FREQUENCY METHOD

The method proposed by Maaø (2007) can be derived by introducing a complex frequency in the diffusive domain Maxwell equations

$$-\nabla\times\boldsymbol{H}(\boldsymbol{x},\omega)+\boldsymbol{\sigma}(\boldsymbol{x})\boldsymbol{E}(\boldsymbol{x},\omega)=-\boldsymbol{J}(\boldsymbol{x},\omega),$$
$$\nabla\times\boldsymbol{E}(\boldsymbol{x},\omega)-i\omega\mu\boldsymbol{H}(\boldsymbol{x},\omega)=-\boldsymbol{K}(\boldsymbol{x},\omega). \quad \text{(A-1)}$$

Using

$$i\omega=i\omega'(1-i\omega'\alpha), \quad \text{(A-2)}$$

which is equation 16 in Maaø (2007), gives

$$-\nabla\times\boldsymbol{H}(\boldsymbol{x},\omega)+\boldsymbol{\sigma}(\boldsymbol{x})\boldsymbol{E}(\boldsymbol{x},\omega)=-\boldsymbol{J}(\boldsymbol{x},\omega),$$
$$\nabla\times\boldsymbol{E}(\boldsymbol{x},\omega)-i\omega'(1-i\omega'\alpha)\mu\boldsymbol{H}(\boldsymbol{x},\omega)=-\boldsymbol{K}(\boldsymbol{x},\omega). \quad \text{(A-3)}$$

By

$$\boldsymbol{E}'(\boldsymbol{x},\omega')=\boldsymbol{E}(\boldsymbol{x},\omega),$$
$$\boldsymbol{H}'(\boldsymbol{x},\omega')=(1-i\omega'\alpha)\boldsymbol{H}(\boldsymbol{x},\omega),$$
$$\boldsymbol{J}'(\boldsymbol{x},\omega')=(1-i\omega'\alpha)\boldsymbol{J}(\boldsymbol{x},\omega),$$
$$\boldsymbol{K}'(\boldsymbol{x},\omega')=\boldsymbol{K}(\boldsymbol{x},\omega), \quad \text{(A-4)}$$

equation A-3 becomes

$$-\nabla\times\boldsymbol{H}'(\boldsymbol{x},\omega')+(1-i\omega'\alpha)\boldsymbol{\sigma}(\boldsymbol{x})\boldsymbol{E}'(\boldsymbol{x},\omega)=-\boldsymbol{J}'(\boldsymbol{x},\omega'),$$
$$\nabla\times\boldsymbol{E}'(\boldsymbol{x},\omega')-i\omega'\mu\boldsymbol{H}'(\boldsymbol{x},\omega)=-\boldsymbol{K}'(\boldsymbol{x},\omega'), \quad \text{(A-5)}$$

which are equations 9 and 10 in Maaø (2007).

Recall that for the correspondence principle, we have equation 10:

$$-i\omega'=\sqrt{-2i\omega\omega_0}. \quad \text{(A-6)}$$

For the complex frequency method, I introduce

$$\alpha=\frac{1}{\omega_\alpha}, \quad \text{(A-7)}$$

which by equation A-2 becomes

$$-i\omega'=\sqrt{-i\omega 2\omega_\alpha+\omega_\alpha^2}-\omega_\alpha. \quad \text{(A-8)}$$

For a large value of α (ω_α is small compared to ω), I find for the primed frequency in Maaø's system,

$$-i\omega' = \sqrt{-i2\omega\omega_\alpha}, \tag{A-9}$$

which is similar to equation A-6. This result shows that the complex frequency method of Maaø approaches the correspondence principle method if a large value of α is used. The methods are, however, not identical. The complex frequency method will give fields with a diffusive tail in the fictitious time domain. The implication is that simulations based on the correspondence principle method can be terminated at a somewhat earlier time than the complex frequency method. This can save some computer time in pure forward simulation. However, there is a potential benefit of the complex frequency method compared to the correspondence principle method: Processing methods such as 3D inversion can depend on adjoint state modeling. This requires that a difference field representation in the frequency domain be transformed back to the fictitious time domain. It is well known that this is an ill-posed problem with correspondence principle methods. The problems with such a transformation could be smaller if a diffusive component was kept in the Maxwell equations, as is the case with the complex frequency method of Maaø. The transform to the fictitious wave domain for this scheme is discussed by Støren et al. (2008).

APPENDIX B

INDEPENDENCE OF SCALE PARAMETER

The choice of ω_0 gives a scaling of the time axis in the fictitious wave domain. The only limitation on ω_0 is that it is real and larger than zero to give positive and real propagation velocities. Practical choices must ensure the fields have numerical values that preserve accuracy both in the wave simulation and in the transform from the fictitious time t' to the frequency domain for diffusive fields. The q domain representation given by Lee et al. (1989) can be obtained by introducing the timelike parameter q in

$$q = \sqrt{2\omega_0}t'. \tag{B-1}$$

Equation 14 becomes

$$-\nabla\times\boldsymbol{H}'(\boldsymbol{x},q) + \boldsymbol{\sigma}(\boldsymbol{x})\partial_q\left[\frac{\boldsymbol{E}'(\boldsymbol{x},q)}{\sqrt{2\omega_0}}\right] = -\boldsymbol{J}'(\boldsymbol{x},q),$$
$$\nabla\times\left[\frac{\boldsymbol{E}'(\boldsymbol{x},q)}{\sqrt{2\omega_0}}\right] + \mu\partial_q\boldsymbol{H}'(\mathbf{x},q) = -\frac{\boldsymbol{K}'(\boldsymbol{x},q)}{\sqrt{2\omega_0}}, \tag{B-2}$$

which by

$$\boldsymbol{E}''(\boldsymbol{x},q) = \frac{\boldsymbol{E}'(\boldsymbol{x},q)}{\sqrt{2\omega_0}},$$
$$\boldsymbol{H}''(\boldsymbol{x},q) = \boldsymbol{H}'(\boldsymbol{x},q),$$
$$\boldsymbol{J}''(\boldsymbol{x},q) = \boldsymbol{J}'(\boldsymbol{x},q),$$
$$\boldsymbol{K}''(\boldsymbol{x},q) = \frac{\boldsymbol{K}'(\boldsymbol{x},q)}{\sqrt{2\omega_0}}, \tag{B-3}$$

gives

$$-\nabla\times\boldsymbol{H}''(\boldsymbol{x},q) + \boldsymbol{\sigma}(\boldsymbol{x})\partial_q\boldsymbol{E}''(\boldsymbol{x},q) = -\boldsymbol{J}''(\boldsymbol{x},q),$$
$$\nabla\times\boldsymbol{E}''(\boldsymbol{x},q) + \mu\partial_q\boldsymbol{H}''(\boldsymbol{x},q) = -\boldsymbol{K}''(\boldsymbol{x},q). \tag{B-4}$$

Equation 17 becomes

$$E_i(\boldsymbol{x},\omega) = \int_0^Q dq E_i''(\boldsymbol{x},q)e^{-\sqrt{\frac{\omega}{2}}q}e^{i\sqrt{\frac{\omega}{2}}q}, \tag{B-5}$$

with Q sufficiently large to include the important arrivals. Equation 18 becomes

$$J_n(\boldsymbol{x},\omega) = \frac{1}{\sqrt{-i\omega}}\int_0^Q dq J_n''(\boldsymbol{x},q)e^{-\sqrt{\frac{\omega}{2}}q}e^{i\sqrt{\frac{\omega}{2}}q}. \tag{B-6}$$

APPENDIX C

THE TRANSFORM FROM THE FICTITIOUS WAVE DOMAIN TO THE DIFFUSIVE FREQUENCY DOMAIN

The diffusive Green's function in the frequency domain for a whole-space is well known (Ward and Hohmann, 1987). The x-component of the Green's function resulting from an infinitesimal electric dipole in the x-direction is

$$G_{xx}^{EJ}(\boldsymbol{x},\omega) = -i\omega\mu\frac{e^{ik_\omega r}}{4\pi r}\left[\left(\frac{x^2}{r^2}-1\right)+\left(3\frac{x^2}{r^2}-1\right)\left(\frac{i}{k_\omega r}-\frac{1}{(k_\omega r)^2}\right)\right], \tag{C-1}$$

where $k_\omega = \sqrt{i\mu\sigma\omega}$ and $r = \sqrt{x^2+y^2+z^2}$.

Deriving the wave-domain electric field resulting from an infinitesimal electric dipole in the x-direction is straightforward. The vector potential for the nonconductive case $\boldsymbol{A}(\boldsymbol{x},t)$ is given in Ward and Hohmann (1987). The electric field can be expressed as

$$\boldsymbol{E}(\boldsymbol{x},t) = -\nabla\Phi(\boldsymbol{x},t) - \partial_t\boldsymbol{A}(\boldsymbol{x},t), \tag{C-2}$$

where $\Phi(\boldsymbol{x},t)$ is a scalar potential. The Lorenz gauge condition relates the vector and scalar potential,

$$\nabla\boldsymbol{A}(\boldsymbol{x},t) = -\mu\varepsilon\partial_t\Phi(\boldsymbol{x},t) = -\frac{1}{c^2}\partial_t\Phi(\boldsymbol{x},t). \tag{C-3}$$

I introduce the source polarization $\boldsymbol{P}$ by $\boldsymbol{J}(\boldsymbol{x},t) = \partial_t\boldsymbol{P}(\boldsymbol{x},t)$ so for the x-component,

$$P_x(\boldsymbol{x}_s,t) = \delta(\boldsymbol{x}-\boldsymbol{x}_s)\Gamma(t). \tag{C-4}$$

The x-component of the electric field caused by an infinitesimal electric dipole in the x-direction is then

$$E_x(\boldsymbol{x},t) = \frac{\mu}{4\pi r}\left[\left(\frac{x^2}{r^2}-1\right)\partial_t^2\Gamma(t-r/c)+\left(3\frac{x^2}{r^2}-1\right)\times\left(\frac{c}{r}\partial_t\Gamma(t-r/c)+\frac{c^2}{r^2}\Gamma(t-r/c)\right)\right]. \tag{C-5}$$

The above solution is general. An FDTD simulation of equation 4 or equation 14 in a whole-space results in the above electric field.

Equation C-5 gives the response in the fictitious wave domain if the propagation velocity is $c = \sqrt{2\omega_0/\mu\sigma}$. I use equation C-5 to obtain a Green's function in the form of equation 20. Thus, I write the electric field in equation C-5 as $E_x'(\boldsymbol{x},t')$ and perform the transform in equation 17. I also need the transformed time function for the source in equation 19.

I assume that the polarization source time function $\Gamma(t')$ is a Gaussian so that the current source time function is the time derivative of a Gaussian,

$$\Gamma(t') = \sqrt{\frac{\beta}{\pi}} e^{-\beta(t'-t_0)^2}. \tag{C-6}$$

The frequency-domain representation of $\Gamma(t')$ in the fictitious wave domain is

$$\Gamma(\omega'') = e^{-\frac{\omega''^2}{4\beta}} e^{i\omega'' t_0}, \tag{C-7}$$

where I have used a double prime on the angular frequency to mark that the spectrum is analyzed in the fictitious wave domain. The angular frequency ω'' is then real. The maximum frequency in the wave domain is given by β. This frequency determines the dispersion properties of the FDTD simulation in the fictitious wave domain. Thus, $\Gamma(t')$ will approach a temporal Dirac delta distribution in the limit $\beta \to \infty$. Appropriate choices for finite-difference simulations where a maximum allowed frequency f_{max} is already given as

$$\beta \approx \pi f_{\max}^2. \tag{C-8}$$

A proper choice of t_0 is required to make the signal close to causal. A lower limit for finite-difference simulations can be

$$t_0 \geq \frac{\pi}{f_{\max}}. \tag{C-9}$$

However, the following derivation is performed without choosing the value of β. The only assumption is that the pair β and t_0 give a causal function in the sense that any integral contributions from $t' = -\infty$ to $t' = 0$ can be neglected.

The frequency transform of the transmitter current (equation 19) is required by equation 20. Thus, I need

$$\int_0^T dt' \partial_{t'} \Gamma(t') e^{i\omega' t'} = -i\omega' e^{i\omega' t_0} e^{-i\frac{\omega\omega_0}{2\beta}}. \tag{C-10}$$

The diffusive domain representation for the transmitter current is

$$J_x^T(\omega) = 2\omega_0 e^{-\sqrt{\omega\omega_0}t_0} e^{i\sqrt{\omega\omega_0}t_0} e^{-i\frac{\omega\omega_0}{2\beta}}. \tag{C-11}$$

For the transform of $E_x'(\boldsymbol{x},t')$, I need

$$\begin{aligned}
&\int_0^T dt' \Gamma(t'-r/c) e^{i\omega' t'} = e^{i\omega'(t_0+r/c)} e^{-i\frac{\omega\omega_0}{2\beta}},\\
&\int_0^T dt' \partial_{t'} \Gamma(t'-r/c) e^{i\omega' t'} = -i\omega' e^{i\omega'(t_0+r/c)} e^{-i\frac{\omega\omega_0}{2\beta}},\\
&\int_0^T dt' \partial_{t'}^2 \Gamma(t'-r/c) e^{i\omega' t'} = -\omega'^2 e^{i\omega'(t_0+r/c)} e^{-i\frac{\omega\omega_0}{2\beta}},
\end{aligned} \tag{C-12}$$

with the relations

$$\begin{aligned}
\frac{i\omega'}{c} &= ik_\omega,\\
i\omega' c &= \frac{2\omega\omega_0}{k_\omega},\\
c^2 &= \frac{2i\omega\omega_0}{k_\omega^2}.
\end{aligned} \tag{C-13}$$

Note above in equations C-10 and C-12 that as a result of the transform β now appears in a phase factor only. The parameter β, which determines the frequency spectrum in the fictitious wave domain, does not determine the frequency spectrum in the diffusive domain. Thus, the choice of the maximum frequency in the fictitious wave domain does not influence the maximum frequency in the diffusive domain.

The diffusive domain representation for E_x' is

$$\begin{aligned}
E_x(\boldsymbol{x},\omega) = E_x'(\boldsymbol{x},\omega') = &-i\omega\mu\frac{e^{ik_\omega r}}{4\pi r}\left[\left(\frac{x^2}{r^2}-1\right)+\left(3\frac{x^2}{r^2}-1\right)\right.\\
&\left.\times\left(\frac{i}{k_\omega r}-\frac{1}{(k_\omega r)^2}\right)\right]\\
&\times 2\omega_0 e^{-\sqrt{\omega\omega_0}t_0} e^{i\sqrt{\omega\omega_0}t_0} e^{-i\frac{\omega\omega_0}{2\beta}}.
\end{aligned} \tag{C-14}$$

Observe that $J_x^T(\omega)$ from equation C-11 is a factor in equation C-14 so that by equation 20 the Green's function becomes

$$\begin{aligned}
G_{xx}^{EJ}(\boldsymbol{x},\omega) = \frac{E_x(\boldsymbol{x},\omega)}{J_x^T(\omega)} = &-i\omega\mu\frac{e^{ik_\omega r}}{4\pi r}\left[\left(\frac{x^2}{r^2}-1\right)\right.\\
&\left.+\left(3\frac{x^2}{r^2}-1\right)\left(\frac{i}{k_\omega r}-\frac{1}{(k_\omega r)^2}\right)\right],
\end{aligned} \tag{C-15}$$

which is equal to equation C-1. One result here is that the transform from the fictitious time domain to the diffusive frequency domain gives a result in which the spectrum of the diffusive domain electric field in equation C-14 is independent of the spectrum of the field in the fictitious wave domain. The spectrum of the electric field in the fictitious wave domain is controlled by the parameter β. This parameter gives a phase correction only in equation C-14 and no influence on the spectrum of the diffusive domain electric field. Further on, this phase correction is not present for the Green's function in equation C-15 because it is removed by the normalization with the source current. Another result is that dependence on the scale parameter ω_0 disappears after the deconvolution that is dictated by equation 20.

REFERENCES

Berenger, J. P., 1994, A perfectly matched layer for the absorption of electromagnetic waves: Journal of Computational Physics, **114**, 185–200.

Carcione, J. M., 2006, A spectral numerical method for electromagnetic diffusion: Geophysics, **71**, no. 1, I1–I9.

Cerjan, C., D. Kosloff, R. Kosloff, and M. Reshef, 1985, A nonreflecting boundary condition for discrete acoustic and elastic wave equations: Geophysics, **50**, 705–708.

Commer, M., and G. A. Newman, 2006, An accelerated time domain finite difference simulation scheme for three-dimensional transient electromagnetic modeling using geometric multigrid concepts: Radio Science, **41**, RS3007.

Dablain, M. A., 1986, The application of high-order differencing to the scalar wave equation: Geophysics, **51**, 54–66.

Davydycheva, S., V. Druskin, and T. Habashy, 2003, An efficient finite-dif-

ference scheme for electromagnetic logging in 3D anisotropic inhomogeneous media: Geophysics, **68**, 1525–1536.
de Hoop, A. T., 1996, A general correspondence principle for time-domain electromagnetic wave and diffusion fields: Geophysical Journal International, **127**, 757–761.
Eidesmo, T., S. Ellingsrud, L. M. MacGregor, S. Constable, M. C. Sinha, S. Johansen, F. N. Kong, and H. Westerdahl, 2002, Sea bed logging (SBL): A new method for remote and direct identification of hydrocarbon filled layers in deepwater areas: First Break, **20**, 144–152.
Ellingsrud, S., T. Eidesmo, M. C. Sinha, L. M. MacGregor, and S. Constable, 2002, Remote sensing of hydrocarbon layers by SeaBed Logging (SBL): Results from a cruise offshore Angola: The Leading Edge, **21**, 972–982.
Gabrielsen, P. T., I. Brevik, R. Mittet, and L. O. Løseth, 2009, Investigating the exploration potential for 3D CSEM using a calibration survey over the Troll Field: First Break, **27**, 67–75.
Gazdag, J., 1981, Modeling the acoustic wave equation with transform methods: Geophysics, **46**, 854–859.
Gershenson, M., 1997, Simple interpretation of time-domain electromagnetic sounding using similarities between wave and diffusion propagation: Geophysics, **62**, 763–774.
Holberg, O., 1987, Computational aspects of the choice of operator and sampling interval for numerical differentiation in large-scale simulation of wave phenomena: Geophysical Prospecting, **37**, 629–655.
Kosloff, D., and R. Kosloff, 1986, Absorbing boundaries for wave propagation problems: Journal of Computational Physics, **63**, 363–376.
Lee, K. H., G. Liu, and H. F. Morrison, 1989, A new approach to modeling the electromagnetic response of conductive media: Geophysics, **54**, 1180–1192.
Løseth, L. O., and B. Ursin, 2007, Electromagnetic fields in planarly layered anisotropic media: Geophysical Journal International, **170**, 44–80.
Maaø, F. A., 2007, Fast finite-difference time-domain modeling for marine-subsurface electromagnetic problems: Geophysics, **72**, no. 2, A19–A23.
Oristaglio, M. L., and G. W. Hohmann, 1984, Diffusion of electromagnetic fields into a two-dimensional earth: A finite-difference approach: Geophysics, **49**, 870–894.
Srnka, L. J., J. J. Carazzone, M. S. Ephron, and E. A. Eriksen, 2006, Remote reservoir resistivity mapping: The Leading Edge, **25**, 972–975.
Støren, T., J. J. Zach, and F. A. Maaø, 2008, Gradient calculations for 3D inversion of CSEM data using a fast finite-difference time-domain modelling code: 70th Annual Conference and Exhibition, EAGE, Extended Abstracts, P194.
Tarantola, A., 1984, Inversion of seismic reflection data in the acoustic approximation: Geophysics, **49**, 1259–1266.
Wang, T., and G. W. Hohmann, 1993, A finite-difference, time-domain solution for three-dimensional electromagnetic modeling: Geophysics, **58**, 797–809.
Ward, S. H., and G. W. Hohmann, 1987, Electromagnetic theory for geophysical applications: *in* M. N. Nabighian, ed., Electromagnetic methods in applied geophysics — Theory, SEG, 131–311.
Yee, K. S., 1966, Numerical solution of initial boundary value problems involving Maxwell's equations in isotropic media: IEEE Transactions on Antennas and Propagation, **14**, 302–307.